

A Short-lived Rejuvenation during the Decades-long Changing-look Transition in the Nucleus of Mrk 1018

KAI-XING LU,^{1,2} YAN-RONG LI,³ QINGWEN WU,⁴ LUIS C. HO,^{5,6} ZHI-XIANG ZHANG,⁷ HAI-CHENG FENG,^{1,2} SHA-SHA LI,^{1,2} YONG-JIE CHEN,³ MOUYUAN SUN,⁷ XINWEN SHU,⁸ WEI-JIAN GUO,⁹ CHENG CHENG,¹⁰ JIAN-GUO WANG,^{1,2} DONGCHAN KIM,¹¹ JIAN-MIN WANG,³ AND JIN-MING BAI^{1,2}

¹Yunnan Observatories, Chinese Academy of Sciences, Kunming 650011, China

²Key Laboratory for the Structure and Evolution of Celestial Objects, Chinese Academy of Sciences, Kunming 650011, China

³Key Laboratory for Particle Astrophysics, Institute of High Energy Physics, Chinese Academy of Sciences, 19B Yuquan Road, Beijing 100049, China

⁴Department of Astronomy, School of Physics, Huazhong University of Science and Technology, Luoyu Road 1037, Wuhan, China

⁵Kavli Institute for Astronomy and Astrophysics, Peking University, Beijing 100871, China

⁶Department of Astronomy, School of Physics, Peking University, Beijing 100871, China

⁷Department of Astronomy, Xiamen University, Xiamen, Fujian 361005, China

⁸Department of Physics, Anhui Normal University, Wuhu, Anhui 241002, China

⁹National Astronomical Observatories, Chinese Academy of Sciences, 20A Datun Road, Chaoyang District, Beijing 100101, China

¹⁰Chinese Academy of Sciences South America Center for Astronomy, National Astronomical Observatories, CAS, Beijing 100101, China

¹¹National Radio Astronomy Observatory, 520 Edgemont Road, Charlottesville, VA 22903, USA

ABSTRACT

Changing-look active galactic nuclei (CL-AGNs), characterized by emerging or disappearing of broad lines accompanied with extreme continuum flux variability, have drawn much attention for their potential of revealing physical processes underlying AGN evolution. We perform seven-season spectroscopic monitoring on Mrk 1018, one of the earliest identified CL-AGN. Around 2020, we detect a full-cycle changing-look transition of Mrk 1018 within one year, associated with a nucleus outburst, which likely arise from the disk instability in the transition region between the outer standard rotation-dominated disk and inner advection-dominated accretion flow. Over the past forty-five years, the accretion rate of Mrk 1018 changed 1000 times and the maximum Eddington ratio reached 0.02. By investigating the relation between broad-line properties and Eddington ratio ($L_{\text{bol}}/L_{\text{Edd}}$), we find strong evidence that the full-cycle type transition is regulated by accretion. There exists a turnover point in the Balmer decrement, which is observed for the first time. The broad Balmer lines change from a single peak in Type 1.0-1.2 to double peaks in Type 1.5-1.8 and the double-peak separation decreases with increasing accretion rate. We also find that the full width at half maximum (FWHM) of the broad Balmer lines obeys $\text{FWHM} \propto (L_{\text{bol}}/L_{\text{Edd}})^{-0.27}$, as expected for a virialized BLR. The velocity dispersion σ_{line} follows a similar trend in Type 1.5-1.8, but displays a sharp increases in Type 1.0-1.2, resulting in a dramatic drop of $\text{FWHM}/\sigma_{\text{line}}$. These findings suggest that a virialized BLR together with accretion-dependent turbulent motions might be responsible for the diversity of BLR phenomena across AGN population.

Keywords: Active galactic nuclei (16); Supermassive black holes (1663); Accretion (14); Time domain astronomy (2109); Reverberation mapping (2019)

1. INTRODUCTION

It is generally acknowledged that active galactic nuclei (AGNs) emit substantial energy from accretion of matter onto supermassive black holes (SMBHs) via an accretion disk (AD), leading to a wealth of observational features across the electromagnetic spectrum (e.g., Ho 2008; Netzer 2015). The broad-line region (BLR), situated in the outer part of the accretion disk and the inner region of the dust

torus, generates broad emission lines with varying strengths, velocity widths, and profile shapes, manifesting as a prominent feature in optical and ultraviolet spectra. The BLR plays a vital role in accurately determining SMBH masses and understanding AGN evolution (e.g., Netzer 2013; Elitzur et al. 2014; Zhou et al. 2019; Lu et al. 2022). Nevertheless, the structure and origin of the BLR remain subjects of considerable debate.

AGNs can be typically classified by the relative strength of the broad emission lines compared to narrow lines (e.g., the flux ratio of broad $H\beta$ to $[\text{O III}]\lambda 5007$ lines), such as types 1.0, 1.2, 1.5, 1.8, and 2.0 (Osterbrock 1977), which

respectively correspond to $H\beta/[O\ III]>5$, $5>H\beta/[O\ III]>2$, $2>H\beta/[O\ III]>0.33$, $H\beta/[O\ III]<0.33$, and no broad emission lines (Winkler 1992). The unification model posits that all AGNs share a similar structure, comprising an accreting SMBH surrounded by a dusty toroidal configuration (dust torus) and the diversity in AGN types arises from the different viewing angles (Antonucci 1993; Urry & Padovani 1995). However, Changing-look events (CLEs) in AGNs, often referred as changing-look active galactic nuclei (CL-AGNs), exhibit significant continua variability along with transitions between AGN types over time scales much shorter than viscous time of accretion disks (Khachikian & Weedman 1971; Penston & Perez 1984; Cohen et al. 1986; Wang et al. 2024), posing challenges to the viewing angle-dependent unification model.

CL-AGNs are further categorized into changing-obscuration AGNs (CO-AGNs) and changing-state AGNs (CS-AGNs) based on the distinct physical processes indicated by X-ray and optical/ultraviolet observations (Ricci & Trakhtenbrot 2023). In CO-AGNs, CLEs observed in X-ray bands are primarily driven by changes in the column density along the line of sight (Matt et al. 2003; Meregheiti et al. 2021). In contrast, for CS-AGNs, CLEs in the optical and ultraviolet are typically linked to significant variations in the radiation field driven by accretion (e.g., Sheng et al. 2017; Graham et al. 2020). Recently, hundreds of CL-AGNs have been detected through the spectral characteristics of broad emission lines that either emerge (turn on) or vanish (turn off) (e.g., MacLeod et al. 2016; Yang et al. 2018; Graham et al. 2020; Zeltyn et al. 2024; Guo et al. 2024a,b), yet only a limited number have shown recurring changing-look phenomena based on infrequent spectral observations over several decades (Wang et al. 2024; Komossa et al. 2024), such as Mrk 1018 (Cohen et al. 1986; McElroy et al. 2016; Lyu et al. 2021), Mrk 590 (Denney et al. 2014), NGC 4151 (Shapovalova et al. 2010; Chen et al. 2023a; Feng et al. 2024), NGC 2617 (Moran et al. 1996; Shappee et al. 2014; Feng et al. 2021), and NGC 1566 (Oknyansky et al. 2019). These changes correspond to transitions between different AGN types (from Type 1 to Type 1.2/1.5, Type 1.8/1.9, or Type 2 and vice versa). Significant efforts have been made to uncover the mechanisms behind these changes (e.g., Husemann et al. 2016; Krumpe et al. 2017; Sheng et al. 2017; Kim et al. 2018; Sniegowska et al. 2020; Lyu et al. 2021; Liu et al. 2021; Veronese et al. 2024). Notably, in the case of 1ES 1927+654, Li et al. (2022) suggested that the substantial change in accretion rate was due to a tidal disruption event (TDE; also see Merloni et al. 2015). However, the feeding mechanisms for SMBHs remain largely unresolved in most instances (e.g., Gaspari et al. 2020). Nonetheless, understanding of the changing-look process remains elusive, as a complete cycle of such transitions has not yet been thoroughly observed. Continuous monitoring of CL-AGNs could provide valuable insights into the AGN structure evolution, thereby unveiling the key physical mechanism of CLAGNs.

Over the past few decades, numerous observational methods have been established to investigate the internal structure

of AGNs. One notable method, spectroscopic reverberation mapping (SRM), has proven to be an effective approach for analyzing the geometry and dynamics of the BLR in AGNs, as well as for estimating the masses of SMBHs (e.g., Blandford & McKee 1982; Peterson 1993). SRM has revealed that the BLR exhibits a stratified structure, with the radii of low-ionization line emitters being approximately ten times larger than those of high-ionization lines (Bentz et al. 2010), aligning with the predictions of photoionization models. The Balmer decrement, which is the ratio of the fluxes of Balmer lines ($H\alpha/H\beta$), serves as an indicator of internal reddening in AGNs since the intrinsic Balmer decrement remains constant for a specific gas composition, such as the Case B recombination value of $H\alpha/H\beta\sim 2.74$ (Osterbrock & Ferland 2006). In observations, however, the typical Balmer decrement value tends to exceed the intrinsic value (e.g., around 3.1, Lu et al. 2019c). Additionally, the Balmer decrement can help examine the ionization effects within the BLR (Korista & Goad 2004; Wu et al. 2023; Li et al. 2024). Monitoring variations in the continuum color is a widely employed technique for studying AGN variability and heating processes. Some studies have noted that the nucleus spectra of AGNs tend to be bluer when brighter from the multi-band variability data (e.g., Cutri et al. 1985; Sakata et al. 2011; Cai et al. 2016; Guo & Gu 2016; Ren et al. 2022), while mid-infrared spectra of CL-AGNs become redder when brighter (Yang et al. 2018; Graham et al. 2020). The large flux variations in CL-AGNs offer unique opportunity to probe the internal structures of AGNs by carefully studying the SRM, the Balmer decrement, and the color variations.

To study the evolution of AGNs, particularly the accretion disk and broad-line region evolution, we initiated a long-term observational project utilizing the Lijiang 2.4m telescope to conduct spectroscopic monitoring of a carefully selected sample of well-known AGNs. This sample includes prominent reverberation mapping AGNs (e.g., NGC 5548, see Lu et al. 2022), changing-look AGNs (e.g., Mrk 1018, Mrk 590, Mrk 993, and Mrk 883), as well as candidates for SMBH binaries (e.g., SDSS J153636.22+044127.0, which is characterized by double-peaked broad emission lines). Mrk 1018, a merger galaxy classified as Hubble type S0 (Koss et al. 2011; Veronese et al. 2024) at $z=0.043$, was one of the earliest confirmed CL-AGNs based on limited spectroscopic observations. It exhibited a transition from type 1.9 to 1.2 over approximately five years (from 1979 to 1986; Cohen et al. 1986), before reverting back to type 1.9 in 2015 (McElroy et al. 2016). Since 2017, we have conducted follow-up spectroscopic observations of this source. In this paper, we present findings of a full-cycle CLE that occurred around 2020, along with a full-cycle AGN type transition behavior observed in Mrk 1018.

2. OBSERVATION AND DATA

2.1. Optical Spectroscopy and Calibration

Long-term spectroscopic observations of Mrk 1018 were conducted utilizing the Yunnan Faint Object Spectrograph and Camera (YFOSC) attached to the Lijiang 2.4 m tele-

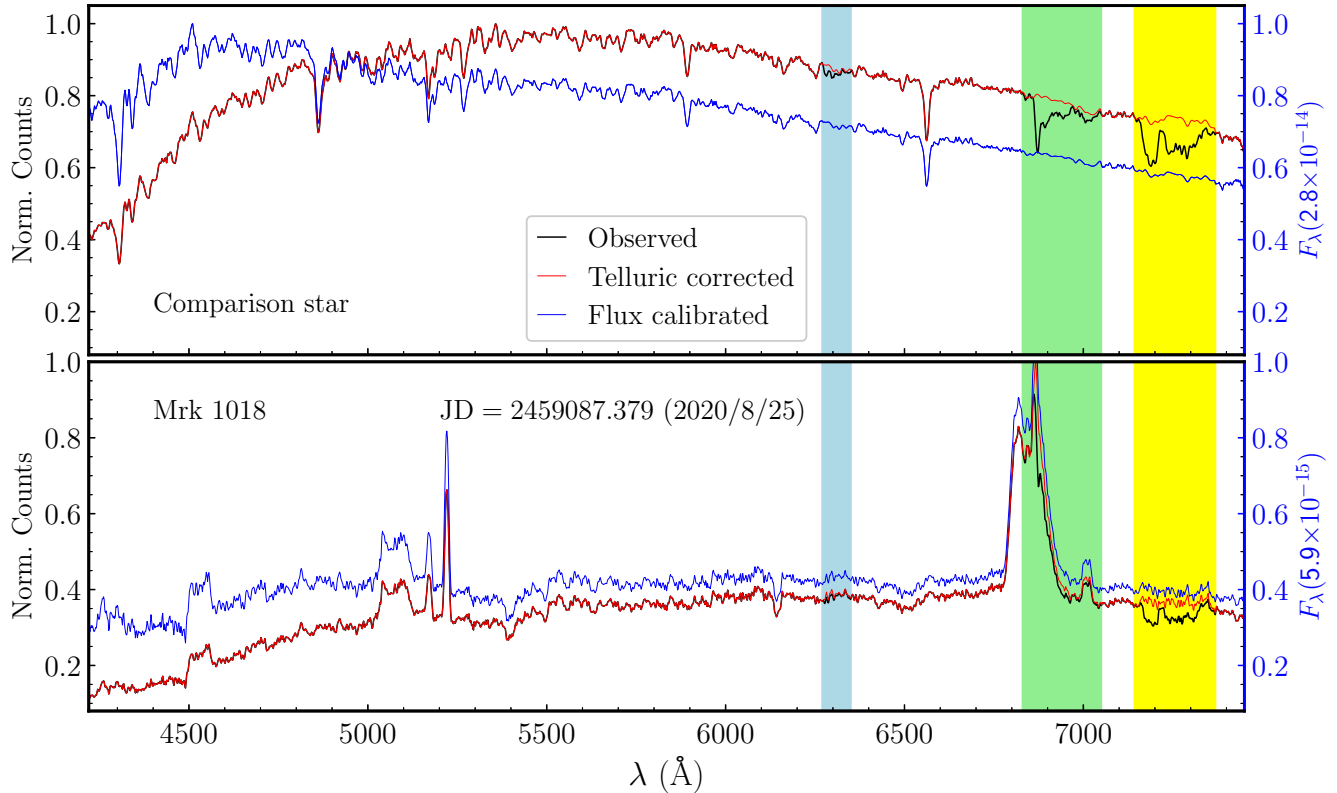


Figure 1. An example of the telluric correction and spectral flux calibration. The top and bottom panels are for the comparison star and Mrk 1018, respectively. In each panel, the black line shows the observed spectra (in counts, left vertical axis), the red line shows the telluric-corrected spectrum, and the blue line shows the flux-calibrated spectrum (in units of $\text{erg s}^{-1} \text{cm}^{-2} \text{\AA}^{-1}$, right vertical axis). The three vertical colored bands represent telluric absorption windows.

scope (LJT). YFOSC is equipped with a back-illuminated 2048×2048 pixel CCD, featuring a pixel size is $13.5 \mu\text{m}$, a pixel scale is $0.283''$ per pixel, a field-of-view is $10' \times 10'$, and a series of filter and Grism (Fan et al. 2015; Wang et al. 2019). For spectroscopy of Mrk 1018, Grism 14 was employed, which spans wavelengths from approximately $\sim 3600 \text{\AA}$ to 7460\AA and offers a dispersion of $1.8 \text{\AA pixel}^{-1}$. Following our earlier studies (Lu et al. 2021a,b, 2022), a long slit with a projected width of $2.5''$ was used, taking into account the average seeing conditions at the observatory.

The spectroscopic monitoring of Mrk 1018 started on November 5, 2017, and to date, seven-season observations have been conducted from November 2017 to February 2024 (with Modified Julian Days ranging from 58063 to 60324). Similar to the long-term spectroscopic monitoring of NGC 5548 (Lu et al. 2022), we rotated the long slit within the field of view to simultaneously capture spectra of Mrk 1018 and a nearby stable comparison star. This observational approach is commonly employed in reverberation mapping campaigns, where the spectra of the comparison star can provide high-precision spectral calibration, including flux calibration and telluric absorption corrections (e.g., see Hu et al. 2015; Lu et al. 2019a, 2021b and below). Standard neon and helium lamps were used for wavelength calibration. In total, we

acquired 96 spectroscopic observations over an approximate duration of seven years.

We processed the two-dimensional spectroscopic data using the standard procedures in PyRAF. This involved bias subtraction, flat-field correction, wavelength calibration, and the removal of cosmic ray. Subsequently, all spectra were extracted with a consistent extraction window after subtracting the sky background. We opted for a relatively narrow extraction window of 20 pixels ($5.7''$), which aids in minimizing Poisson noise from sky background and increasing the signal-to-noise (S/N) ratio of the spectra. The sky background was estimated from two adjacent regions ($+7.4'' \sim +14''$ and $-7.4'' \sim -14''$) located on either side of the extraction window.

The red side of ground-based optical spectrum is contaminated by the variable absorptions of the telluric atmosphere. In the observed spectrum of Mrk 1018, there are three telluric absorption windows, which are marked by vertical colored bands in Figure 1. One of these windows (the green band) overlaps with the broad $\text{H}\alpha$ line. We first correct the telluric absorption and subsequently calibrate the spectral fluxes.

Following the work of Lu et al. (2021b), we processed the observed spectra of Mrk 1018 through a three-step calibration procedure. First, we determined the synthesis stellar template for the comparison star by aligning its observed

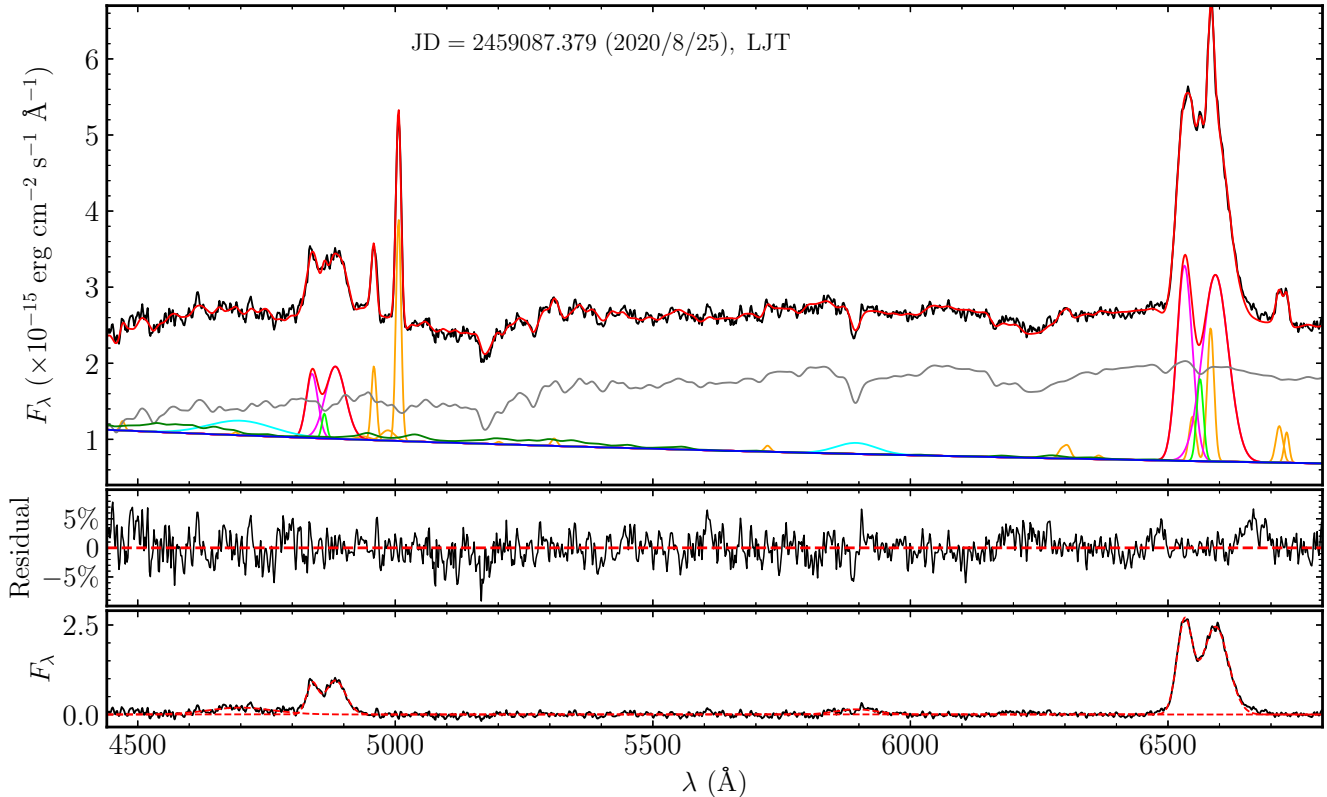


Figure 2. An example of multicomponent fitting and decomposition of the spectrum. The fitting model includes a power law ($f_{\lambda} \propto \lambda^{\alpha}$, α is the spectral index) for the AGN continuum (blue), an iron template for the iron multiplets (green), a stellar template for the host-galaxy starlight (gray), two double Gaussians for each broad Balmer line ($H\beta$ and $H\alpha$, magenta), single Gaussian for each narrow Balmer line ($H\beta$ and $H\alpha$, lime), single Gaussian for each Helium broad line ($He\ II\ \lambda 4686$ and $He\ I\ \lambda 5876$, cyan), two double Gaussians for the $[O\ III]$ doublets (orange), single Gaussian for the $[S\ II]$ doublets and the $[N\ II]$ doublets (orange), and other narrow emission lines.

spectrum with a library of synthesis stellar models (e.g., Husser et al. 2013). Next, we modeled the observed spectra of comparison star (in counts) using the chosen stellar template, while masking the telluric absorption bands during this modeling (i.e., the regions marked by color diagram in Figure 1). We then derived the telluric transmission spectra by dividing the observed spectrum of the comparison star by the modeled spectrum. This allowed us to use the telluric transmission spectra to adjust for the telluric absorption lines in each of the observed spectra. Figure 1 (left y-axis) displays the corrected spectra of telluric absorption (in red) alongside the observed spectra (in black), with the bottom panel representing the spectrum of Mrk 1018 and the top panel showing the spectrum of the comparison star. Finally, similar to the previous step, we generated a wavelength-dependent sensitivity function for each object/comparison star pair by comparing the telluric-corrected spectrum of the comparison star with the stellar template. This sensitivity function was then utilized to calibrate the spectrum of Mrk 1018 (see also Lu et al. 2019a, 2021a, 2022). The flux-calibrated spectra of Mrk 1018 (bottom panel) and its comparison star (top panel) are shown in blue in Figure 1 (right y-axis).

Before our monitoring, there exist nine spectra concurrently covering the broad $H\beta$ and $H\alpha$ lines (Kim et al. 2018;

Osterbrock 1981; Cohen et al. 1986; Abazajian et al. 2009; Jones et al. 2009; Trippe et al. 2010; McElroy et al. 2016), which enable us to investigate the extensive long-term spectral evolution of Mrk 1018 (see Section 3.4). We obtained these early spectra from Kim et al. (2018) and recalibrated them by assuming the same $[O\ III]\lambda 5007$ flux as our spectra. The first spectra of Mrk 1018 was taken in the 1970s, meaning that our spectroscopic baseline spans more than 45 years.

2.2. Spectral Fitting and Measurements

The spectral fitting scheme is commonly adopted in spectral analysis of AGNs to separate the blending components (e.g., Dong et al. 2011; Park et al. 2012; Guo & Gu 2014; Barth et al. 2015). In line with previous fitting routine (e.g., Lu et al. 2022), we conducted the spectral fitting and multicomponent decomposition to extract the spectral characteristics of Mrk 1018 (see Figure 2), including variability and velocity shifts of broad emission lines. To cover the broad $H\beta$ and $H\alpha$ regions while minimizing degrees of freedom, we set the fitting window from 4440 Å to 6800 Å in rest frame for all Mrk 1018 spectra. The fitting includes the following components: (1) A power law ($f_{\lambda} \propto \lambda^{\alpha}$, α is the spectral index) representing the AGN continuum. (2) An iron template from

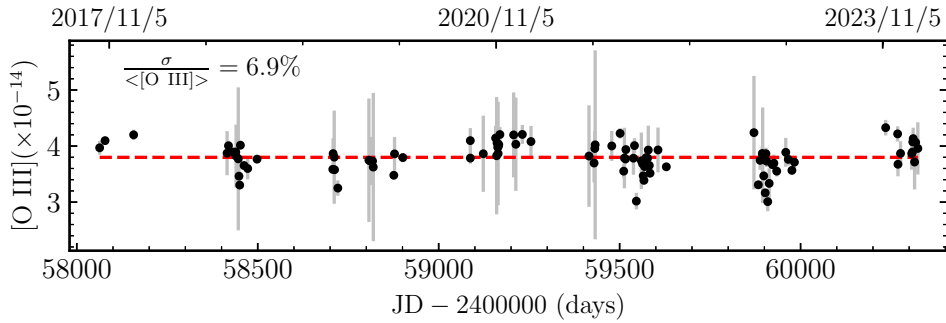


Figure 3. The light curve of the [O III] $\lambda 5007$ in the LJT observation period. The red dashed line represents the mean flux ($3.8 \times 10^{-14} \text{ erg s}^{-1} \text{ cm}^{-2}$).

Boroson & Green (1992) for the iron multiplets. (3) A stellar template with an age of 11 Gyr and metallicity of $Z = 0.05$ from Bruzual & Charlot (2003) to account for the host-galaxy starlight. (4) Double Gaussians for each broad Balmer lines ($H\beta$ and $H\alpha$). In practice, we initially attempted to fit the broad Balmer line using double Lorentzians (Lorentzian was employed for the broad Balmer line of Narrow-Line Seyfert 1 galaxies, see Véron-Cetty et al. 2001), but found the fits are inferior compared to those using double Gaussians for the double-peak broad lines. Therefore, we chose to use double Gaussians to model the broad Balmer lines. (5) Two sets of double Gaussians for the [O III] doublets $\lambda 5007/\lambda 4959$. (6) A single Gaussian for each narrow emission line. (7) Four sets of single Gaussian for the [S II] doublets and the [N II] doublets. All components were fitted simultaneously across the fitting window using the MPFIT package (Markwardt 2009), which employs the Levenberg–Marquardt algorithm for χ^2 -minimization. During the spectral fitting for each spectrum, the flux ratio of the [O III] doublets was fixed to the theoretical value of 3 (e.g., McGill et al. 2008; Hu et al. 2015); all the narrow emission lines were tied to the same velocity and shift, while the rest of the fitting parameters were allowed to vary. Various host-galaxy templates from Bruzual & Charlot (2003) were also evaluated and the template with an age of 11 Gyr and a metallicity $Z = 0.05$ provided a reasonable fit for the spectral index of AGNs continuum ($\sim \lambda^{-1.5}$) and the stellar absorption lines. While several iron templates have been proposed for fitting the optical or ultraviolet spectra of AGNs (e.g., Boroson & Green 1992; Véron-Cetty et al. 2004; Kovačević et al. 2010; Park et al. 2022), we found that the spectral fitting of Mrk 1018 is not sensitive to the choice of the specific iron template.

Next, we focus on the measurements of spectral characteristics. The broad $H\beta$ and $H\alpha$ lines fluxes for each spectrum are measured from the optimal fitted models and are tabulated in Table 1 along with the uncertainties (including Poisson errors and systematic errors). The fluxes of the AGNs continuum can be measured from the best-fitted power-law component at 5100 \AA . During our observation period, the pseudo-continuum is dominated by the starlight from the host galaxy. The mild degeneracy between power-law continuum and host-galaxy component will cause scatter to the obtained AGN continuum at 5100 \AA . Therefore, we just use the av-

Table 1. The fluxes of broad Balmer lines

JD (-2,400,000 days)	$H\beta$ ($10^{-14} \text{ erg s}^{-1} \text{ cm}^{-2}$)	$H\alpha$ ($10^{-14} \text{ erg s}^{-1} \text{ cm}^{-2}$)
Previous observations		
44097.500	0.855 ± 0.070	7.453 ± 0.108
45958.500	14.711 ± 0.124	33.368 ± 0.185
51812.500	9.685 ± 0.139	31.777 ± 0.138
53199.500	9.063 ± 0.185	29.738 ± 0.153
54350.500	20.599 ± 0.146	38.452 ± 0.177
54416.500	20.221 ± 0.142	40.974 ± 0.157
55182.500	9.268 ± 0.079	29.589 ± 0.107
55538.500	9.514 ± 0.083	29.190 ± 0.118
57032.500	1.041 ± 0.059	5.889 ± 0.085
Our seven-season monitoring		
58063.136	0.725 ± 0.114	3.174 ± 0.284
58078.118	0.956 ± 0.103	3.448 ± 0.282
58157.048	0.966 ± 0.109	3.208 ± 0.284
58415.239	0.116 ± 0.121	2.635 ± 0.286

NOTE—The spectral sources and measurements refer to Section 2.1 and 2.2, respectively. (This table is available in its entirety in machine-readable form.)

eraged AGN continuum flux at 5100 \AA as a reference for the intercalibration of different photometric light curves (see Section 2.3). We measure the flux of [O III] $\lambda 5007$ line from the best-fitted model and report the result in Figure 3, which exhibits a scatter of 6.9%. This level of scatter indicates a sufficient accuracy in our spectral calibration.

In spectral fitting described above, the broad $H\beta$ and $H\alpha$ lines in each observation are well modeled by two Gaussian components. This allows us to extract the characteristics of the broad Balmer lines from the optimal models. After correcting the wavelength shift of broad Balmer lines, which usually arise from varying seeing and mis-centering, using its narrow lines as wavelength reference, we measure the peak separations of two Gaussian components (including broad $H\beta$ and $H\alpha$ lines) based on the differences in peak wavelengths. Additionally, we measure the line widths in-

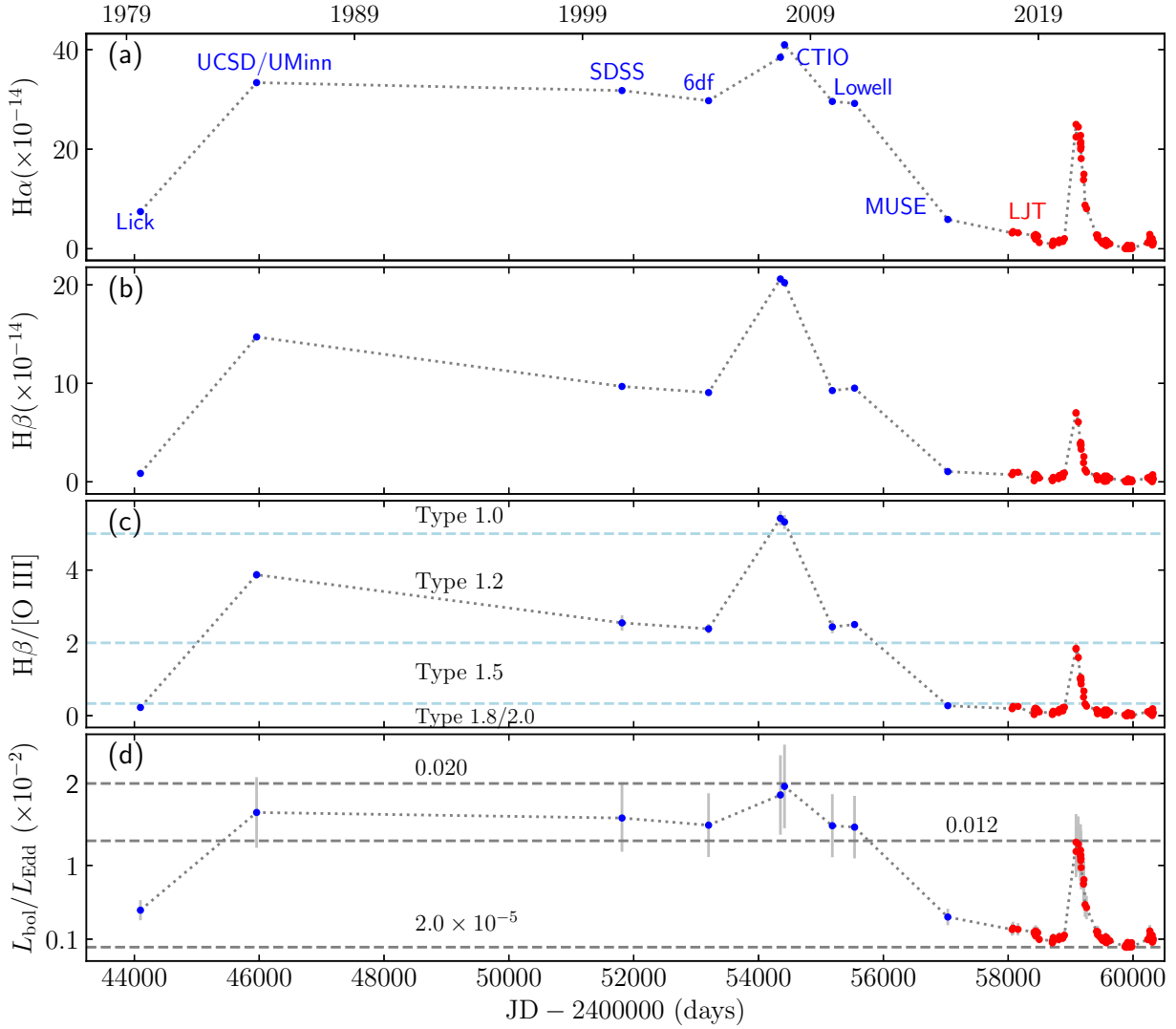


Figure 4. Long-term variability of Mrk 1018 from 1979 to 2024 for (a) the $H\alpha$ flux, (b) the $H\beta$ flux, (c) the flux ratio $H\beta/[O\text{ III}]\lambda 5007$ (indicating the type transition), and (d) the Eddington ratio. The $H\alpha$ and $H\beta$ fluxes are in units of $\text{erg s}^{-1} \text{cm}^{-2}$. The earlier data are in blue and the LJT data are in red.

cluding full-width at half-maximum (FWHM) and velocity dispersion (σ_{line}) for broad $H\beta$ and $H\alpha$ lines. To reasonably determine the FWHM of the double-peaked emission line, we identify a blue-side peak and a red-side peak within the line profile, and the FWHM is calculate from the maximum wavelength separation of these peaks at each half-maximum, as described by Peterson et al. (2004). In practice, instrument broadening is coupled with varying atmospheric (seeing) broadening, so we estimate the total broadening of the broad emission line for each observation by comparing the width of the $[O\text{ III}]\lambda 5007$ line with that from the SDSS spectrum, which is then used to derive the broadening-corrected line width. These measurements will be used to investigate the broad-line properties in subsequent analyses.

2.3. Optical Photometry and Intercalibration

To obtain the long-term variability of Mrk 1018, we compiled the photometry data from the public archival database of Zwicky Transient Facility (ZTF; Graham et al. 2019) and Asteroid Terrestrial-impact Last Alert System (ATLAS; Tonry et al. 2018). We use the ZTF g - and r -band data, along with the ATLAS c - and o -band data, and combine them using the Python package PyCALI¹ (Li et al. 2014), which employs a multiplicative factor and an additive factor to intercalibrate different sources of light curves. We adopt ZTF- g as the reference dataset and align other datasets with it.

2.4. Mid-infrared Photometry

Mrk 1018 is also covered by the Wide-field Infrared Survey Explorer (WISE; Wright et al. 2010) survey. We re-

¹ <https://github.com/LiyiAstroph/PyCALI>

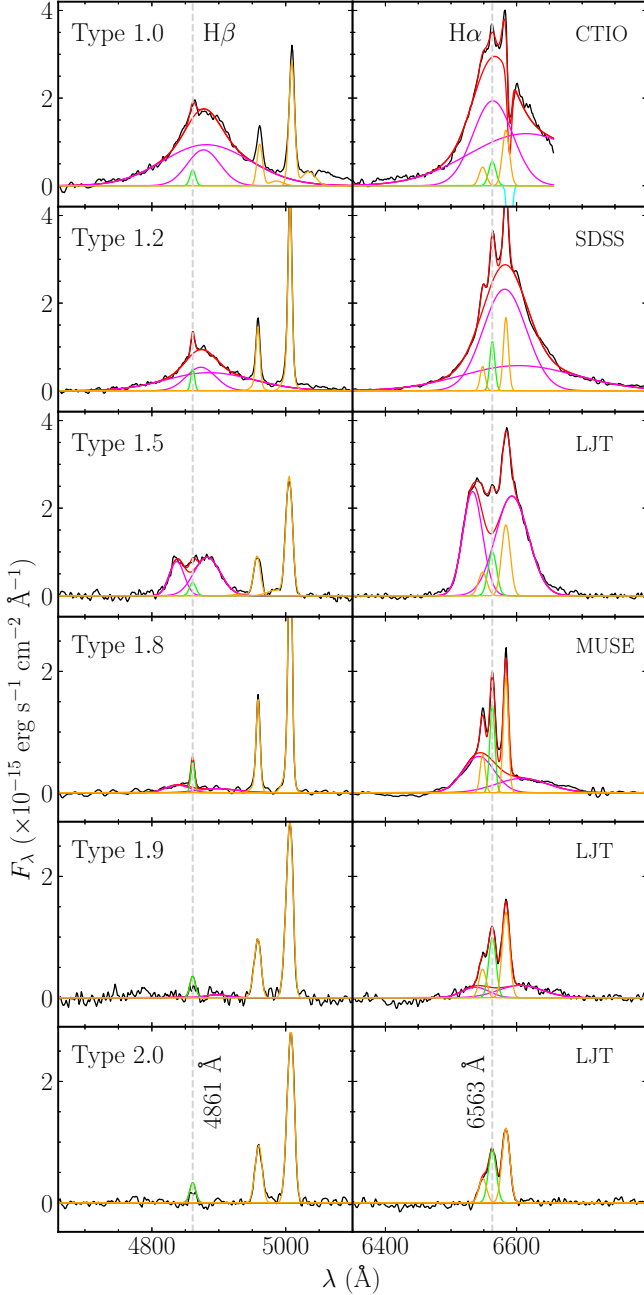


Figure 5. Evolution of the $H\beta$ and $H\alpha$ line profiles. Each row of panels displays the characteristic profiles of different types, with the broad $H\beta$ in the left and $H\alpha$ in the right. The black curve shows the original data, the magenta curves show the broad-line components, the orange curves show $[\text{O III}]\lambda 4959/\lambda 5007$ lines in the $H\beta$ region and $[\text{N II}]\lambda 6548/\lambda 6583$ lines in the $H\alpha$ region, and the lime curves show the narrow $H\beta$ and $H\alpha$. We add an absorption component in the fitting of the CTIO spectra (top right panel, in cyan). The types, including 1.0, 1.2, 1.5, 1.8, 1.9 and 2.0 (no broad $H\beta$ and $H\alpha$ lines), are marked in the left panels and the spectral sources are marked in the right panels. The wavelength shifts for the broad $H\beta$ and $H\alpha$ regions are corrected using the narrow $H\beta$ and $H\alpha$ lines, respectively.

trieved the photometric data with the following flags: the best

frame image quality score ($qi_fact = 1$), no contamination of scattered light from the moon ($moon_masked = 0$), the larger South Atlantic Anomaly separation ($saa_sep \geq 5$), and spurious detections excluded ($cc_flags = 0$). When necessary, we convert $W1$ and $W2$ magnitudes into flux densities by adopting zero-point flux densities $F_\lambda(W1 = 0) = 8.03 \times 10^{-12} \text{ erg s}^{-1} \text{ cm}^{-2} \text{ \AA}^{-1}$ and $F_\lambda(W2 = 0) = 2.43 \times 10^{-12} \text{ erg s}^{-1} \text{ cm}^{-2} \text{ \AA}^{-1}$ (Jarrett et al. 2013). The resulting fluxes and magnitudes are rebinned every 6 months.

3. DATA ANALYSIS AND RESULTS

The light curves for broad $H\alpha$ and $H\beta$ lines, along with the spectral sources (panels a and b), and the variations of AGN type characterized by line ratio of broad $H\beta$ and $[\text{O III}]\lambda 5007$ (panel c) are illustrated in Figure 4. By applying the relationship between the optical luminosity (L_{5100}) and broad $H\alpha$ luminosity ($L_{H\alpha}$) established by Greene & Ho (2005), represented as $L_{5100} = 2.39 \times 10^{43} (L_{H\alpha}/10^{42})^{0.86} \text{ erg s}^{-1}$, we can obtain the optical luminosity for each observation. Furthermore, using the relation $L_{\text{bol}} = 9.8 L_{5100}$ (McLure & Dunlop 2004), we derive the bolometric luminosity of $L_{\text{bol}} = 2.34 \times 10^{44} (L_{H\alpha}/10^{42})^{0.86} \text{ erg s}^{-1}$, which allows us to estimate the bolometric luminosity for each observation. Finally, using the Eddington luminosity $L_{\text{Edd}} = 1.26 \times 10^{38} (M_{\text{BH}}/M_\odot) \text{ erg s}^{-1}$, we estimate the Eddington ratio ($L_{\text{bol}}/L_{\text{Edd}}$) from the derived bolometric luminosity, and show its variations in panel (d) of Figure 4. The details on the estimation of SMBH mass and Eddington luminosity refer to Section 3.2. To inspect the change of broad emission line, we select and present the typical emission line spectra in Figure 5, focusing on the broad $H\alpha$ and $H\beta$ regions and covering types 1.0, 1.2, 1.5, 1.8, 1.9 and 2.0. In columns (2-4) of Table 2, we list the typical values for the broad $H\alpha$ line fluxes and related parameters, including the minimum and maximum values, as well as the values as $H\beta/[\text{O III}]\lambda 5007 = 0.1$. This ratio of 0.1 nearly represents the detection threshold for broad $H\beta$ lines due to their flux being comparable to that of narrow $H\beta$ lines. Additionally, we calculate the logarithm ratios of narrow line ratios using all observations from LJT, specifically $[\text{O III}]\lambda 5007/H\beta$ and $[\text{N II}]\lambda 6584/H\alpha$, for each observation, yielding 0.18 ± 0.03 and 1.01 ± 0.01 , respectively, indicating Mrk 1018 is a Seyfert galaxy (Kewley et al. 2001). These findings reveal that the Eddington ratio of Mrk 1018 has varied by a factor of 1000 over the last 45 years of observation, implying a significant modification of the central engine, and reflecting a transition from passive to active states in the SMBH. Consequently, Mrk 1018 serves as an exemplary target for investigating the physical processes underlying AGN evolution.

3.1. Multi-scale Outburst and Accretion Physics

During the observation period at LJT, we find that Mrk 1018 exhibited a significant outburst around 2020 (see Figure 4). To explore multi-band variability, we gathered archival photometric data for optical and mid-infrared band

Table 2. The broad H α line fluxes and derived parameters

Parameters	1979-2024			Outburst around 2020		
	(JD 2,444,097 to 2,460,324)			(JD \sim 2,458,900 to \sim 2,459,300)		
	Minimum	H β /[O III] λ 5007=0.1	Maximum	Before the outburst	Peak	After the outburst
(1)	(2)	(3)	(4)	(5)	(6)	(7)
H α Flux (10^{-14} erg s $^{-1}$ cm $^{-2}$)	0.01	0.75	40.97	1.32	24.97	1.41
H α Luminosity (10^{40} erg s $^{-1}$)	0.05	3.26	177.84	5.73	108.39	6.12
Luminosity at 5100 Å (10^{42} erg s $^{-1}$)	0.004	1.26	39.21	2.04	25.70	2.16
Bolometric Luminosity (10^{43} erg s $^{-1}$)	0.04	1.23	38.43	2.00	25.08	2.12
Eddington ratio	2.0×10^{-5}	6.1×10^{-4}	0.020	1.0×10^{-3}	0.012	1.0×10^{-3}

NOTE—Columns (2-4) are the relevant parameters observed between 1979 and 2024 (JD 2,444,097 to 2,460,324), while columns (5-7) represent the outburst phase around 2020 (JD \sim 2,458,900 to \sim 2,459,300, also see Table 3). The optical luminosity of $L_{5100}=2.39 \times 10^{43} (L_{H\alpha}/10^{42})^{0.86}$ erg s $^{-1}$ was given by Greene & Ho (2005), where $L_{H\alpha}$ denotes the luminosity of broad H α line. Using the relation of $L_{bol}=9.8L_{5100}$ (McLure & Dunlop 2004), we derive the bolometric luminosity of $L_{bol}=2.34 \times 10^{44} (L_{H\alpha}/10^{42})^{0.86}$ erg s $^{-1}$. Here, the cosmology with $H_0 = 72$ km s $^{-1}$ Mpc $^{-1}$, $\Omega_\Lambda = 0.7$, and $\Omega_M = 0.3$ is adopted.

as described above. The results are shown in the left panels of Figure 6 alongside the light curves of broad emission lines. The optical light curves include the ZTF g -, r -, and merged $g&r$ -bands and the mid-infrared light curves include WISE $W1$ - and $W2$ -bands. Multi-band light curves distinctly present the outburst feature of Mrk 1018 around 2020, rising abruptly within a timescale of about two hundred days from the long-term dimming state (see Figure 4). In columns (5-7) of Table 2, we present the typical values of the broad H α line fluxes and related parameters during the outburst, including the maximum values and those measured before and after but near the outburst. We find that the Eddington ratio changed more than 12 times throughout the outburst phase. In addition, the light curve of [O III] λ 5007, depicted in Figure 3 with a minor scatter of 6.9% indicates that there is no variability in [O III] λ 5007. This finding suggests that the emissions from narrow-line region (NLR) are unaffected by the outburst event, or that the outburst did not introduce new components into the NLR.

In order to quantify the characteristics of the outburst, we attempted to model the light-curve profiles of the outburst using various functions after detrending, identifying the Gaussian function as the most suitable model, the results are reported in panel (a) of Figure 6. The details regarding the fitting processes and arguments refer to Section 4.3 and Appendix A and B. The typical timescales of multi-band outburst (e.g., $T=2 \times 2.35\sigma$) and peak times (t_{peak}) were calculated from the modelings and are summarized in Table 3. We find that the multi-scale outburst timescales exhibit the relation $T_g < T_{H\beta} < T_{H\alpha} < T_{W1} < T_{W2}$, while the peak times follow $t_{peak,g} < t_{peak,H\beta} < t_{peak,H\alpha} < t_{peak,W1} < t_{peak,W2}$, where the subscripts denote different bands or broad emission lines (see Figure 6). These relations demonstrate that the multi-scale variabilities during the outbursts in Mrk 1018 are interrelated with different time delays and also suggest that the timescales and peak times increase with

greater physical distance from the central SMBH, aligning with the echo phenomenon.

The color–magnitude diagram is a widely used tool for examining AGN variability. Many efforts have explored the color–magnitude relation for CL-AGNs, revealing that their optical spectra exhibit a bluer-when-brighter behavior, while mid-infrared spectra show a redder-when-brighter trend (e.g., Sheng et al. 2017; Yang et al. 2018; Graham et al. 2020). Using Gaussian modelings, we have constructed the optical and mid-infrared color–magnitude diagrams for the outburst phase, as displayed in Figure 7 (see Appendix B for details). Indeed, the optical and mid-infrared variations show different trends in Mrk 1018.

In the optical band, we observed a bluer-when-brighter trend, aligning with findings in normal AGNs. This implies that the mechanisms underlying extreme variability in CL-AGNs are likely analogous to those responsible for the stochastic variability observed in normal AGNs. The maximum variation in optical color reaches $\Delta_{color}=0.47$ mag, alongside a significant flux increase by a factor of 17 for broad lines (a proxy of the UV continuum), indicating that the nucleus spectrum becomes much bluer during outburst. However, the nucleus still has a low accretion rate even at the peak of the outburst ($L_{bol}/L_{Edd} \sim 0.012$). It is important to note that although the rising phase of the outburst lacks data, the declining phase are well captured, with the results from this stage actually confirming these certain relations at least.

Many models of variability could account for the extreme outburst, as discussed in details by Brogan et al. (2023). In summary, a clumpy accretion disk could function on a viscous timescale, yet fails to match the outburst duration (about a year). Quasi-periodic eruptions can be linked to a warped accretion disk model, but we do not detect quasi-periodic outbursts during our monitoring period. Tidal Disruption Events (TDE), occurring when a star wanders close to a SMBH, can produce a short and dramatic outburst; however, the light-

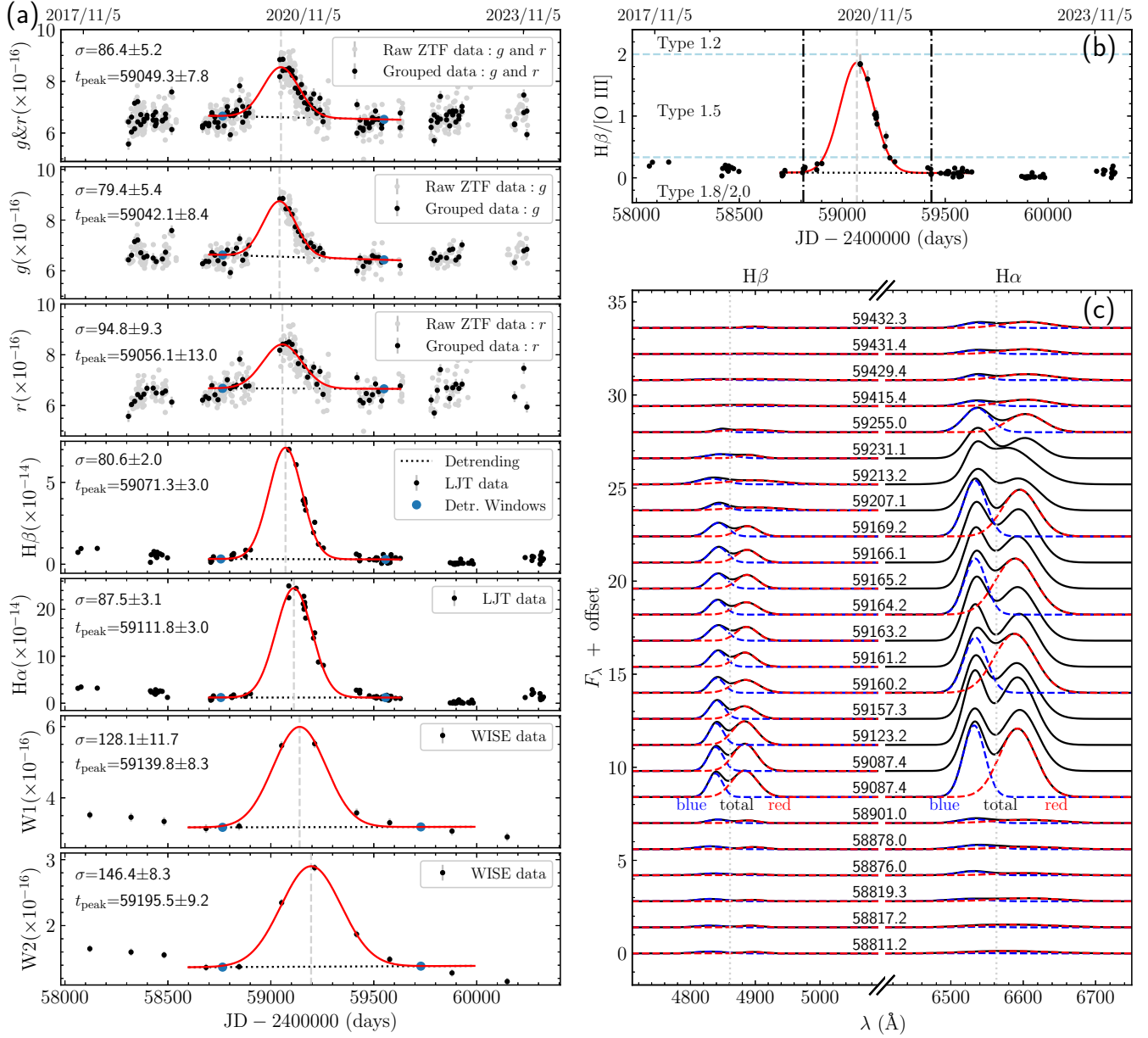


Figure 6. Multi-scale outbursts accompanied by a short-lived yet full-cycle changing-look transition in Mrk 1018. Panel (a) displays the light curves of ZTF photometry (combined $g&r$ -, g -, and r -band, in units of $\text{erg s}^{-1} \text{cm}^{-2} \text{\AA}^{-1}$), the broad Balmer lines ($H\beta$ and $H\alpha$, in units of erg s cm^{-2}), as well as the WISE photometry ($W1$ - and $W2$ -band, in units of $\text{erg s}^{-1} \text{cm}^{-2} \text{\AA}^{-1}$). After subtracting a linear trend determined from the adjacent regions around the outburst (blue circles indicating the centers of chosen detrending windows, and dotted lines representing linear trends), the light-curve profiles of the outburst are fitted using a Gaussian (in red), yielding a typical $\chi^2/\text{dof} \sim 2$. The vertical dashed line shows the peak position of the outburst (t_{peak}). The fitting parameters, including σ (days) and t_{peak} (-2,400,000 days), are noted in each sub-panel. Panel (b) presents the variations in AGN type, where the type-transition profile is also modeled by a Gaussian (in red) that shares the same parameters as the broad $H\beta$ modeling. The broad $H\beta$ and $H\alpha$ line profiles within vertical dot-dashed lines are showed in panel (c). Panel (c) shows the fitted broad $H\beta$ and $H\alpha$ line profiles for the outburst period, they are marked by the observation time of JD (-2,400,000 days), which increases from the bottom to the top. The pronounced double-peaked shape highlights the broad-line feature, with the total broad lines (in black) representing the best fitted model, composed of a blue-shifted Gaussian (in blue dashed lines) and a red-shifted Gaussian (in red dashed lines).

curve profiles of the outburst in Mrk 1018 cannot be fitted by a typical power-law model associated with TDEs (also see Brogan et al. 2023). Besides, during the dimming phase, the nucleus’s spectrum become significantly reddens, in conflict with the color variations expected from TDEs (for additional arguments see Section 3.3). The chaotic cold accretion of SMBHs, potentially linked to the viscous process, also fails to explain the outburst timescale. Our findings challenge all these models.

It is generally accepted that the central engine of low-accretion/low-luminosity AGNs (e.g., those below a characteristic accretion rate of $\sim 1\%$ of Eddington ratio) consist of an inner hot advection-dominated accretion flow (ADAF, Abramowicz et al. 1995) and an outer truncated cold rotation-dominated thin disk (SSD, Shakura & Sunyaev 1973; Ho 2008). The central engine of Mrk 1018 likely aligns with this two-component accretion disk model, as it overall stays below the 1% Eddington limit during both the outburst and past 45 years of observations (see Table 2). Based on this model, a radiation pressure instability may occur in a narrow transition region between the two components (Sniegowska et al. 2020), potentially leading to short-timescale outbursts and inducing changing-look behavior. This variability model actually applies in a viscous framework, predicting that the nucleus’s spectrum should become significantly bluer, and its viscous timescale can be shortened by several factors (dependent on the ratio of the transition-region size to its distance from the central SMBH) compared to the viscous timescale of the Shakura-Sunyaev disk (Shakura & Sunyaev 1973). Remarkably, our findings closely align with the predictions of this variability model in light of the outburst timescale and nucleus spectrum. Another competing mechanism is the Bondi accretion of unstable surrounding gases during the transition between active and passive SMBHs (Wang et al. 2024). We find that the changing-look timescale observed for Mrk 1018 in this study can be explained by a sudden inflow of surrounding gases within the Bondi accretion radius, situated between the BLR and the NLR (see Equation 3 of Wang et al. 2024).

In the mid-infrared band, we detected the color transitions occurred in the rising/dimming phases. Specifically, the mid-infrared spectrum shows an apparent redder-when-brighter relation when the flux is below approximately half of the maximum value, while it transitions to a bluer-when-brighter relation when the flux crosses this threshold (see panels (ba) to (bd) in Figure 7). This contrasts with earlier findings showing a monotonically redder-when-brighter trend in the mid-infrared spectrum of CL-AGNs (Sheng et al. 2017; Yang et al. 2018; Graham et al. 2020). We noted that these previous results were derived directly from the observed data, as illustrated in the panel (bb) of Figure 7, where the $W1$ - $W2$ vs. $W1$ relation represented by black circles demonstrated the redder-when-brighter relation, and two red circles from the high-luminosity state of the outburst phase appear to disrupt this monotonicity. If the mid-infrared emission at 3.4 and 4.6 μm arise from hot dust heated by AGNs activities (Netzer 2013), the redder-when-brighter trend contra-

Table 3. Characteristics of the outburst

Band/Line	FWHM	Peak (t_{peak})
	(days)	(JD-2,400,000 days)
ZTF- $g&r$	207 ± 12	59049 ± 7
ZTF- g	186 ± 12	59042 ± 8
ZTF- r	228 ± 21	59055 ± 12
H β	192 ± 5	59071 ± 3
H α	206 ± 7	59112 ± 3
WISE- $W1$	302 ± 27	59140 ± 8
WISE- $W2$	345 ± 19	59195 ± 9

dicts the viscous heating model of AGNs on the torus. Any star formation occurring within or outside the torus should heated the torus, resulting in a redder emission from the torus with increasing star formation rates, which aligns with the redder-when-brighter interpretation of the mid-infrared spectrum (Yang et al. 2018). However, this explanation does not account for the outburst timescale observed in Mrk 1018, as the stellar heating timescale on $W2$ -band emission region should be comparable to the stellar evolution timescale. Our modeling of the outburst profiles indicates that the $W2$ -band light-curve is broader than that of the $W1$ -band, suggesting a more extended emission region or a smoother emissivity in the $W2$ -band. Consequently, the rise in $W2$ -band flux occurs earlier than that in the $W1$ -band, while the dimming in $W2$ lags behind $W1$, resulting in the mid-infrared color exhibiting a redder-when-brighter trend during low-luminosity states. Interestingly, the mid-infrared bluer-when-brighter relation observed for the first time in relatively high-luminosity states, supports the notion that hot dust is heated by AGN activities (Netzer 2013). This is further supported by the correlation between the mid-infrared outburst and nucleus outburst (see Figure 6).

3.2. Emission Region Sizes and SMBH Mass

During our spectroscopic monitoring of Mrk 1018, the availability of multi-band light curves enabled us to perform reverberation mapping measurements to determine the size of different emission regions in Mrk 1018. Utilizing the interpolated cross-correlation analysis (Sun et al. 2018), we obtained the rest-frame time delays to be 32_{-8}^{+36} days for the broad H β line, 83_{-33}^{+23} days for the broad H α line, 78_{-21}^{+57} days for WISE $W1$ -band, and 158_{-84}^{+56} days for WISE $W2$ -band, all relative to the the combined ZTF $g&r$ -band. The time delays between the mid-infrared band and ZTF $g&r$ band were corrected for the cosmological time dilation and wavelength dependence using the total correction factor of $(1+z)^{\gamma-1}=(1+z)^{-0.24}$ (Chen et al. 2023b). Unfortunately, the seasonal gaps and sparse sampling result in relatively larger uncertainties in the obtained lags. As a verification, from the Gaussian modeling of outburst profile (see Section 3.1,

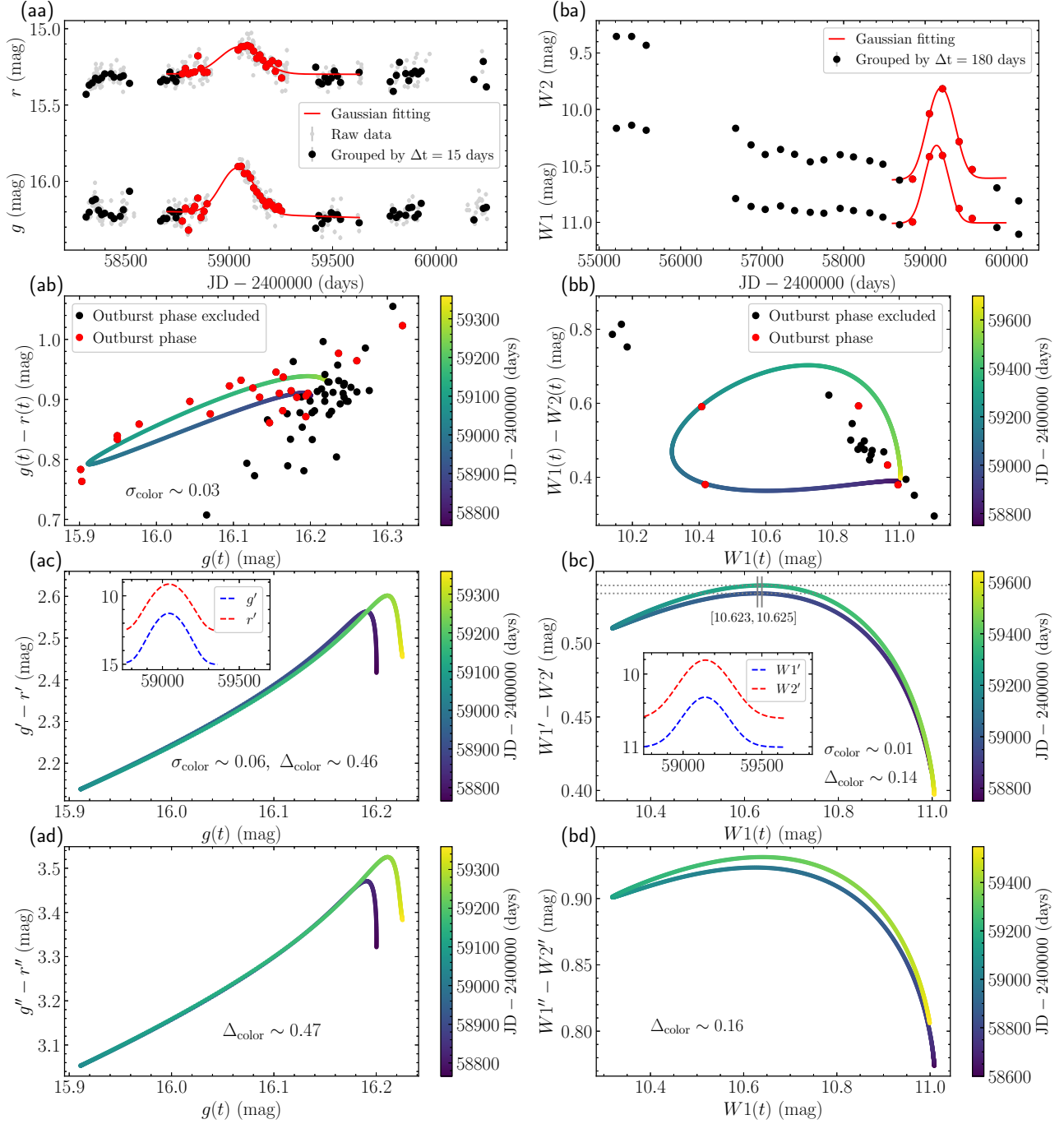


Figure 7. Optical and mid-infrared color–magnitude relations based on the Gaussian fitting model (see Appendix B). The left panels (aa–ad) are for the optical bands, while the right panels (ba–bd) are for the mid-infrared bands. The first row (panels aa and ba) displays the observed (points) alongside the modeled light curves (red lines), with the outburst phase highlighted in red. We calculate the optical and mid-infrared color–magnitude relations in three cases and present in the next three rows, respectively. In the second row (panels ab and bb), the color–magnitude relations are generated directly using the grouped data (where the outburst phase is highlighted in red points) and fitting model of the outburst phase (in colored lines). In the third row (panels ac and bc), because the ZTF g -band covers the broad $H\beta$ lines and ZTF r -band covers the broad $H\alpha$ lines for Mrk 1018 ($z=0.043$), that is the intrinsic optical color is contaminated by delayed broad Balmer lines and also by inter-band time delay, while the intrinsic mid-infrared color is just contaminated by the later. Therefore, the intrinsic optical and mid-infrared color–magnitude relations are derived by eliminating the potential contaminations (see Appendix B for more details), where the inset panel presents the light-curve profiles of the outburst phase that the potential contaminations are eliminated (x -axis is in units of JD-2,400,000 days, and y -axis is in units of magnitudes). In the bottommost row (panels ad and bd), we remove the underlying linear variation trend from the intrinsic color–magnitude relations given above (see Appendix B for more details), then calculate the net optical and mid-infrared color–magnitude relations that reflects the nature of the outburst phase.

4.3 and Appendix A and B), the time delays between different bands can be measured by the offsets in peak times. For the optical continuum variability, we test photometric light curves from ZTF g -, r - and combined $g&r$ -band respectively and only find minor discrepancies in the typical timescales and peak times of the outburst, attributed to the influences of broad emission lines in the passbands. If using the ZTF g -band as the reference, the rest-frame time delays is 28 ± 10 days for the broad $H\beta$ line, 67 ± 10 days for the broad $H\alpha$ line, 97 ± 16 days for WISE $W1$ -band, and 152 ± 17 days for WISE $W2$ -band. It should be noted that the detrending windows used to subtract the underlying flux in the dimming state were chosen to be close to the outburst (JD=2458700 and 2459630 for optical bands and JD=2458600 and 2459990 for mid-infrared bands), however, we find that wider detrending windows do not influence the modeling outcomes. Considering the outburst profiles are effectively modeled by Gaussian functions (see Section 4.3 and Appendix A and B), we tentatively conclude that the above time-delay measurements provide reasonable estimates for the sizes of emission regions.

The virial mass of the SMBH in Mrk 1018 can be estimated using the recipe $M_{\bullet} = f c \tau v^2 / G$, where f represents the virial factor of the BLR, c denotes the speed of light, $c\tau$ indicates the BLR radius measured through reverberation mapping method, v refers to the rotation velocity of the BLR (characterized by the FWHM or velocity dispersion of broad lines), and G is the gravitational constant. From the decomposed broad $H\beta$ lines during the outburst phase (from JD 2458811 to 2459433; see panel (c) of Figure 6), we obtain the average FWHM of broad $H\beta$ line to be $5475 \pm 1313 \text{ km s}^{-1}$ after correcting for the broadening effects (see Section 2.2 for details on line-width measurements), with the uncertainty set by the standard deviation. Using the FWHM and time delay of the broad $H\beta$ line (28 ± 10 days) and adopting $f=1$, we estimate the virial mass of the SMBH in Mrk 1018 (virial-based) to be $M_{\bullet} = (1.64 \pm 0.98) \times 10^8 M_{\odot}$.

The virial SMBH mass relies on the assumption that the BLR is virialized. However, in cases with rapid variability or outbursts, the BLR may not be virialized, leading to unreliable virial mass estimates from broad emission lines. For instance, during the changing-look transition of the true type 2 AGN 1ES 1927+654 over months, Li et al. (2022) found that the time lags of the broad emission lines relative to the optical continuum significantly exceed the radius-luminosity relations (Bentz et al. 2013), and the single-spectrum virial masses (Greene & Ho 2005) were considerably higher than independent measurements using the relation between SMBH masses and the properties of host galaxies. Based on various observational evidence, including a decrease in both continuum flux and line width (which is often seen in TDEs; Holoien et al. 2016; Leloudas et al. 2019), Li et al. (2022) proposed that the SMBH in 1ES 1927+654 had captured a surrounding star (as in TDEs) resulting in a super-Eddington/high accretion system and suggested that its BLR was in the process of formation and rapid evolution, likely not yet virialized. Similarly, the spectral phenomena ob-

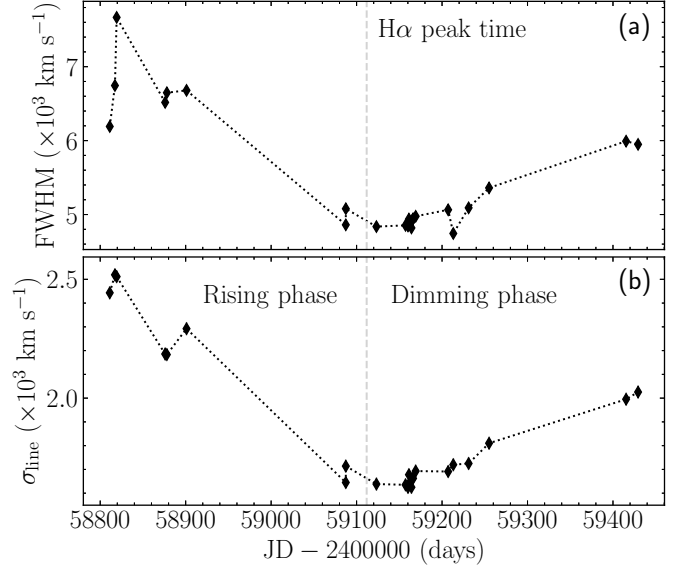


Figure 8. Evolution of the broad $H\alpha$ line width for Mrk 1018 during the outburst phase (JD2,458,811-2,459,433). The panel (a) is for the FWHM and the panel (b) is for σ_{line} . The vertical dashed lines indicate the peak time of the broad $H\alpha$ line. The spectral broadening in each observation, evaluated by comparing line widths of [O III] $\lambda 5007$ from SDSS and LJT spectra, has been corrected (see Section 2.2). We use the line-width scatter of [O III] $\lambda 5007$ as the systematic uncertainty of the broad-line width.

served in Mrk 1018 (as discussed later) resemble those seen in 1ES 1927+654 (Li et al. 2022). This motivates us to examine the evolution of the broad $H\alpha$ line width (FWHM and σ_{line}). As shown in Figure 8, we find that the variations in line widths during the outburst phase align with the normal breathing effect of the BLR, indicating that increased continuum radiation enhances the broad-line emissivity of BLR gases at greater distances, resulting in a decrease in line width with rising continuum emission (and vice versa). This analysis implies that the nucleus outburst of Mrk 1018 did not significantly alter the kinematics of its BLR.

To further verify the virial mass, we utilize the properties of the host galaxy to independently estimate the SMBH mass using the $M_{\bullet} - \sigma_{*}$ relation, where σ_{*} represents the stellar velocity dispersion; Gebhardt et al. 2000; Ferrarese & Merritt 2000). Since no stellar velocity dispersion is available for the bulge of Mrk 1018, we approximate the stellar velocity dispersion by the velocity dispersion of the ionized gas, which is derived from the narrow forbidden emission lines. It has been shown to be approximately valid for a large variety of AGNs (e.g., Nelson & Whittle 1996; Ho 2009; Kong & Ho 2018). We find $\sigma_{\text{gas}} = 176 \text{ km s}^{-1}$ for the [O III] $\lambda 5007$ line from the SDSS spectrum observed in 2000, which provides the highest resolution among all spectra available for Mrk 1018. According to the latest $M_{\bullet} - \sigma_{*}$ relation for early-type galaxies (Greene et al. 2020), we derive $M_{\bullet} = (1.61 \pm 0.41) \times 10^8 M_{\odot}$, remarkably consistent with virial-based SMBH mass. This results in the Edding-

ton luminosity $(2.03 \pm 0.52) \times 10^{46} \text{ erg s}^{-1}$. By combining with the derived bolometric luminosity (see Section 3), we compute the Eddington ratio for each observation, as shown in Figure 4. Over the past 45 years, the Eddington ratio has varied from 2.0×10^{-5} to 0.02, suggesting that Mrk 1018 has been powered by very low accretion rates.

3.3. Full-cycle changing-look transition and type transition

It is generally accepted that a full-cycle changing-look transition should last several decades, which may be linked to the viscous heating timescale of the accretion disk (e.g., Shakura & Sunyaev 1973; Runnoe et al. 2016). However, Our observations show that Mrk 1018 experienced a full-cycle changing-look transition within just one year following a multi-scale outburst. Its type changed from Type 1.8 to Type 1.5/1.2 and then returned to Type 1.8 over the course of the outburst (see panel (b) of Figure 6). Notably, the broad $H\beta$ and $H\alpha$ lines were nearly absent before the outburst, appeared significantly during the outburst, and then almost vanished by the end of the outburst (see panel (c) of Figure 6). The short appearance and rapid disappearance of broad Balmer lines in Mrk 1018 exhibit significant discrepancies with theoretical predictions.

By integrating the archival spectral data, we find that Mrk 1018 has experienced a full-cycle type transition, encompassing sub-types 1.0, 1.2, 1.5, 1.8/1.9 in a continuous manner (see Figure 4 and 5). Our observation from LJT effectively bridge the gap between Type 1.2 and Type 1.8/1.9. We investigate the type transition of Mrk 1018 in relation to the Eddington ratio, as shown in panel (a) of Figure 9, and find a positive correlation between the type transition and Eddington ratio. This shows that strongly varying accretion rate are responsible for regulating the AGN type transitions. Moreover, Mrk 1018 actually represents the first full-cycle observational case, revealing that the intrinsic broad-line emission of AGNs population follows an evolutionary sequence: Type 2-Type1.9/1.8-Type1.5/1.2-Type1 as the accretion rate increases (Stern & Laor 2012a,b; Elitzur et al. 2014).

As demonstrated in IES 1927+654 (Trakhtenbrot et al. 2019; Li et al. 2022), TDEs can act as a trigger for changing-look behavior in AGNs. However, in the case of Mrk 1018, the changing-look transition that took place around 2020 was not induced by a TDE. One reason, as mentioned in Section 3.2, is that the evolution of broad line width during the dimming phase (normal breathing, see Figure 8) contradicts the TDE scenario (typically, the line width decreases with time, while the continuum flux drops; Holoiien et al. 2016; Leloudas et al. 2019). Section 3.1 and Appendix (A and B) present additional reasons. Thus, changing obscuration and changing state remain potential origins for the changing-look behavior of Mrk 1018. The correlations of multi-scale variability effectively rule out the former case since these correlations would be significantly weakened by changing in the covering factor of obstructions along the line of sight (also see Sheng et al. 2017). Furthermore, no ultraviolet and X-ray absorbers have been detected in nucleus of Mrk 1018 over

the past decades (Krumpe et al. 2017; Brogan et al. 2023), which also disfavors the changing obscuration hypothesis. In conclusion, the changing accretion-driven radiation field (or changing-state) might serve as the changing-look mechanism of Mrk 1018, supported by observational evidence of an accretion-dependent full-cycle type transition (see panel (a) of Figure 9).

3.4. Broad-line Properties and BLR Physics

Over the past 45 years, Mrk 1018 has shown significant variability in its broad lines (Figures 4 and 5), providing a unique perspective to study the BLR. Our research reveals that the Balmer decrements have varied significantly from about 1.5 to 9. By analyzing the dependence of the Balmer decrement variations on Eddington ratio, as shown in panel (b) of Figure 9, we find for the first time that the Balmer decrement initially increases and then decreases with increasing Eddington ratio, with a turnover occurring at an Eddington ratio around ~ 0.004 , which roughly corresponds to the transition point between Type 1.8 and Type 1.5. In essence, the Balmer decrement increases to the maximum and then decreases again, a comparable phenomenon has likely been observed in other CL-AGNs (see Figure 13 of Panda & Śniegowska 2024). In Sections 3.3, we argued that the changing obscuration is not the mechanism for the changing-look/type transition in Mrk 1018. Thus, the Balmer decrement serves as an indicator for the ionization effects to the BLR rather than the internal reddening. Previous studies have identified an anti-correlation between Balmer decrement and accretion rate in individual AGNs or normal AGN samples (e.g., Wu et al. 2023; Ma et al. 2023). In the case that there is no nucleus absorption, this anti-correlation can be attributed to the optical depth effects as mentioned in previous studies (e.g., Netzer 1975; Korista & Goad 2004; Wu et al. 2023). This relationship arises because the optical depths of Balmer lines within in the BLR of AGNs are proportional to the ionizing luminosity, where the optical depth in $H\alpha$ is larger than $H\beta$ for a given ionizing luminosity. Interestingly, we have observed for the first time that in Mrk 1018, the Balmer decrement increases to a peak and then decreases (refer to panel (b) of Figure 9). The early theoretical calculations suggested that the variation of Balmer decrement ($H\alpha/H\beta$) in dense environment of AGNs is dependent on the optical depth and exists a turnover, potentially occurring in a range of $60 \leq \tau_{H\alpha} \leq 120$ (see Netzer 1975), where $\tau_{H\alpha}$ denotes the $H\alpha$ optical depth. Our findings provide direct observational support for these theoretical predictions.

Our study shows that the broad $H\beta$ and $H\alpha$ line profiles have significantly changed, evolving from single-peaked profiles in Type 1.0-1.2 phase to double-peaked profiles in Type 1.5-1.8/1.9 phase (see Figure 5). Double-peaked profiles are a hallmark feature of broad Balmer lines during the changing-look transition observed at LJT (in Type 1.5), and the broad $H\beta$ and $H\alpha$ profiles, which exclude the narrow lines, clearly display these features (see Figure 2). Previous studies had shown that those AGNs classified as Type 1.8/1.9, which typically have low-Eddington ratio, frequently

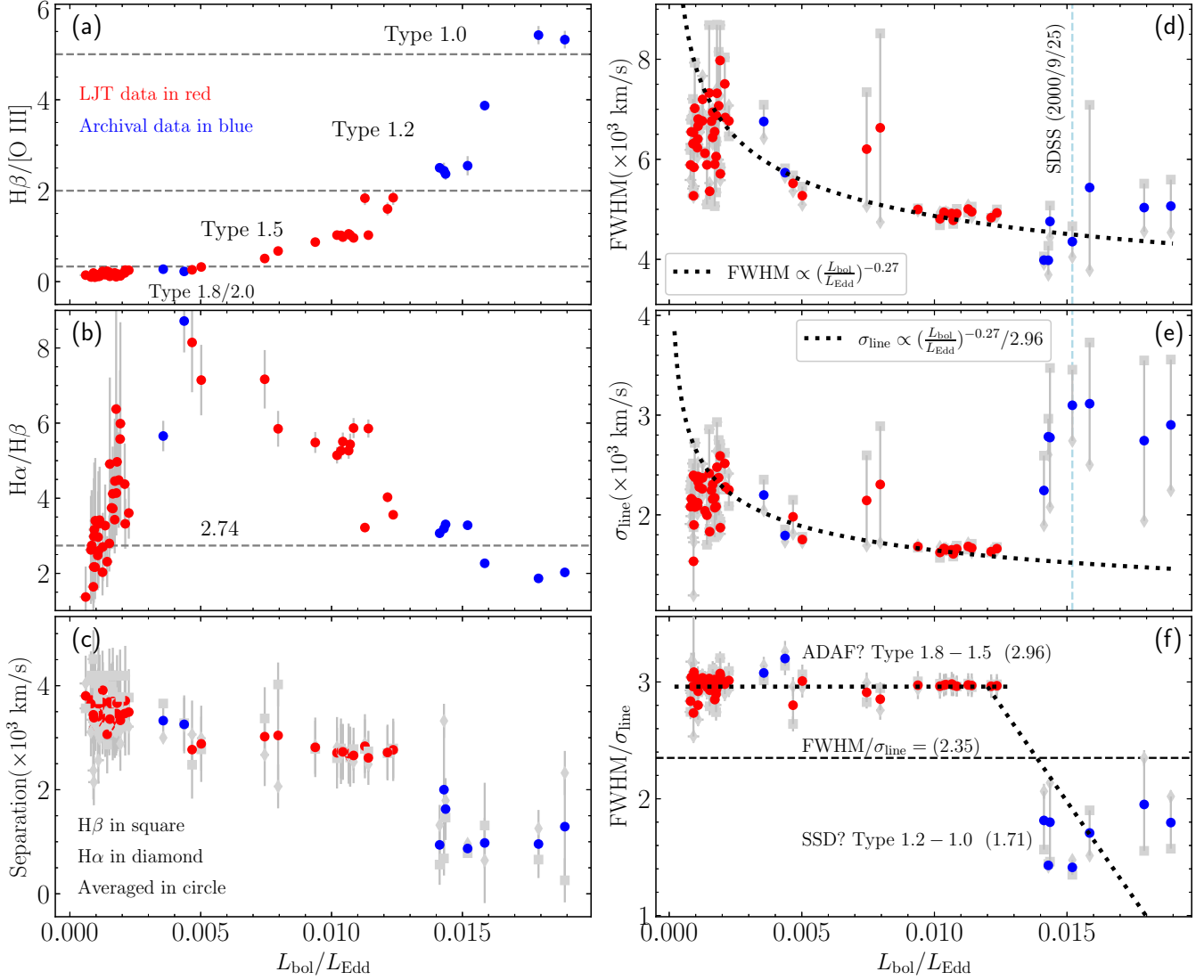


Figure 9. Accretion-dependent type transitions and the broad-line properties in Mrk 1018. The data observed by LJT is shown by red points and the archival data is shown by blue points. Panel (a-c) show the changes of the AGNs type ($H\beta/[O\ III]\lambda 5007$), the Balmer decrement ($H\alpha/H\beta$), and the peak separation of the double-Gaussian broad-line models with the Eddington ratio, respectively. In panel (b), the grey dashed line presents the Baker–Menzel Case B value of 2.74 (Osterbrock & Ferland 2006). In panel (c), the $H\beta$ and $H\alpha$ peak separations are represented by squares and diamonds, respectively, and the average peak separation is shown as points. Panel (d-f) shows changes of the broad $H\beta$ FWHM, the $H\beta$ σ_{line} (velocity dispersion), and the line width ratio $\text{FWHM}/\sigma_{\text{line}}$ with the Eddington ratio, respectively. In panel (f), Type 1.8-1.5 and Type 1.2-1.0 phases, potentially linked to different accretion modes (ADAF and SSD), exhibit distinct $\text{FWHM}/\sigma_{\text{line}}$. Across panels (a-f), to ensure reliable measurements on the parameters, particularly for those involving broad line signals, we select the spectra where the $H\beta/[O\ III]\lambda 5007$ ratio exceeds 0.1. The spectral broadening in each observation (determined by comparing the line width of $[O\ III]\lambda 5007$ in the SDSS and LJT spectra) has been corrected (see Section 2.2).

display double-peaked broad-line profiles, whereas the majority of Type 1.0/1.2 AGNs do not (e.g., Ho et al. 2000; Ho 2008; Strateva et al. 2003; Elitzur et al. 2014). Interestingly, the changes in broad-line profiles of Mrk 1018 is consistent with findings from large-sample analyses. In Section 2.2, we show that all broad $H\beta$ and $H\alpha$ lines observed in the past 45 years can be effectively modeled with two Gaussians (see Figure 2, also see Figure 3 of Kim et al. 2018 for the early spectra). This allows us to derive key parameters

of the broad-line characteristics, such as peak separation and broadening corrected line width of FWHM and σ_{line} . It is known that the shape of broad-line profile can be parameterized by the line-width ratio of FWHM to line dispersion (i.e., $\text{FWHM}/\sigma_{\text{line}}$, see Kollatschny & Zetzl 2011, 2013). A Gaussian profile has a $\text{FWHM}/\sigma_{\text{line}}$ of 2.35, a rectangular profile has a ratio of 3.46, and a Lorentzian profile shows $\text{FWHM}/\sigma_{\text{line}} < 2.35$ (Kollatschny & Zetzl 2011). Below we

explore the BLR properties for Mrk 1018 using these parameters.

The parameters vary by nearly a factor of two and are plotted with Eddington ratio in Figure 9. For the first time, we find that the peak separation decreases with increasing Eddington ratio, with a maximum difference of 2500 km/s (panel (c) of Figure 9). Overall, the FWHM appears to exhibit an exponential decrease as the Eddington ratio rises (panel (d) of Figure 9). Using the virial relation of $\text{FWHM} \propto R_{\text{BLR}}^{-0.5}$ and empirical relation of $R_{\text{BLR}} \propto L_{5100}^{0.533}$ (Bentz et al. 2013), we derive $\text{FWHM} \propto L_{5100}^{-0.27}$, which accordingly leads to $\text{FWHM} \propto (L_{\text{bol}}/L_{\text{Edd}})^{-0.27}$. The dotted curve in panel (d) of Figure 9, along with the observed data, represent this relation. This suggests that the BLR kinematics in Mrk 1018 is consistent with the virial motion and the global kinematics of the BLR is stable (at least in the low-accretion system as Mrk 1018). In practice, the variations in peak separation and FWHM can be attributed to the well-known breathing effect of the BLR. Specifically, an increase in ionizing luminosity from a higher accretion rate enhances the broad-line emissivity of the BLR at larger distances, resulting in a decrease of peak separation along with the decrease in the rotation velocity of the BLR. In addition, the σ_{line} also shows a similar trend as the FWHM (see the dotted line) when the Eddington ratio is below ~ 0.013 (corresponding to Type 1.8-1.5 phase), but it is subject to a sharp rise when the Eddington ratio exceeds 0.013 (corresponding to Type 1.2-1.0 phase; see panel (d) of Figure 9). This implies that a simple breathing effect of the BLR can not fully account for the changes of σ_{line} .

In order to understand the aforementioned differences in the evolution of FWHM and σ_{line} , we turn next to examining the shape of broad line profile, as shown in panel (f) of Figure 9. When the nucleus accretion is below ~ 0.013 times Eddington ratio (in the Type 1.8-1.5 phase), suggesting the nucleus is likely powered by ADAF (Abramowicz et al. 1995), $\text{FWHM}/\sigma_{\text{line}}$ remains constant with an average value of 2.96. This indicates that the broad-line profile approximately resembles a rectangular shape. Conversely, when the nucleus accretion exceeded roughly ~ 0.013 times Eddington ratio (in the Type 1.2-1.0 phase), indicating a probable transition to SSD (Shakura & Sunyaev 1973), $\text{FWHM}/\sigma_{\text{line}}$ sharply drops to an average of 1.71. This suggests that the broad-line profile tends to be a Lorentzian shape. It had been proposed that the dominated broadening mechanism for the broad line profiles arises from Keplerian rotation (implying $\text{FWHM} \propto R_{\text{BLR}}^{-0.5}$ for the virialized BLR), and a Lorentzian shape for the broad line (with $\text{FWHM}/\sigma_{\text{line}} < 2.35$) is attributed to turbulences in the BLR (Osterbrock 1978; Kollatschny & Zetzl 2011, 2013). Consequently, as turbulence in the BLR increases, $\text{FWHM}/\sigma_{\text{line}}$ decreases. As mentioned above, the accretion flow in Mrk 1018 may transition from ADAF to SSD (also see Lyu et al. 2021), where an optically thick geometrically thin disk extends down to the innermost stable circular orbit (Capellupo et al. 2015), resulting in an extended accretion disk. In this scenario, turbulent motions in the outer accretion disk produce a Lorentzian profile, as

suggested by several studies (e.g., Véron-Cetty et al. 2001; Sulentic et al. 2002; Goad et al. 2012).

There are two popular models that can explain the double-peaked nature of broad emission lines. For the first one, based on the failed radiatively accelerated dusty outflow model (FRADO, see Figure 1 of Czerny & Hryniewicz 2011; Naddaf & Czerny 2022), some simulations have shown that the low-ionization broad lines usually present double-peaked profiles when nucleus operates at a few percent of Eddington ratio and transition to single-peaked profiles at high Eddington ratio (Naddaf & Czerny 2022; Wu et al. 2024, submitted). Also, as accretion rate increases, the peak separation decreases. This prediction actually is consistent with our observational finding regarding the peak separation (see panel c of Figure 9). The second model is the Keplerian disk-like model, which also accounts for the occurrence of double-peaked emission lines (Chen & Halpern 1989; Strateva et al. 2003). In practice, these two models may be reconciled by considering an accretion-dependent BLR structure, which has been observed during full-cycle type transition of Mrk 1018 (see Figure 9) and in samples of AGNs (see Elitzur et al. 2014). It is plausible that when the effective temperature of the accretion disk falls below 1000 K, the dusty wind (comprising both BLR gas and dust) resides at the disk's surface (disk-like BLR) before being expelled from the disk and will rise to higher latitudes (bowl-like or spherical BLR) as the temperature increases. This transition results in a change from double-peaked to single-peaked profiles in the broad emission lines. Moreover, as the dusty wind is accelerated to higher latitudes, its turbulence likely increase dramatically, causing a sharp decrease in $\text{FWHM}/\sigma_{\text{line}}$. Our observations in Mrk 1018 lend a support to the dusty-wind model.

In summary, these findings suggest that a virialized BLR together with turbulent motion regulated by the accretion rate or state transition of accretion disk could account for various BLR phenomena observed in AGNs population. Alternatively, some reverberation mapping studies pointed to two distinct components of BLRs (Hu et al. 2020; Nagoshi et al. 2024). For instance, based on reverberation mapping of an extremely variable quasar (SDSS J125809.31+351943.0, J1258), Nagoshi et al. (2024) proposed that the BLR comprises of two distinct emission regions associated with the dusty torus (see Figure 11 of Nagoshi et al. 2024). One region, situated close to the SMBH and potentially at the surface of the accretion disk (as disk-like geometry), is likely formed from accretion related to the dust torus and produce the double-peaked profile. The other region, located relatively farther from the SMBH and possibly at high latitude of accretion disk (as bowl-like geometry), is likely formed by sublimated dust torus, resulting in the single-peaked profile. Nagoshi et al. (2024) further claimed that the broad line emissions of disk-like region might occur independently of the nucleus's activity. However, in the case of Mrk 1018, we observe a strong correlation between the broad line emissions and the varying optical continuum during the double-peaked phase, in conflict with the above scenario of the two-component model.

4. DISCUSSION

4.1. Comparison with the CLE in 1ES 1927+654

Similar to Mrk 1018, the previously recognized true type 2 AGN 1ES 1927+654 (Panessa & Bassani 2002; Tran et al. 2011) underwent an outburst in optical and UV by 4 magnitudes on December 23, 2017. This event, marked by the appearance of broad emission lines after about 100 days, is referred to as a changing-look phenomenon (Trakhtenbrot et al. 2019). Studies have examined the nature of 1ES 1927+654 (Trakhtenbrot et al. 2019; Li et al. 2022; Laha et al. 2022), focusing on the feeding mechanisms of the central engine and the formation of the broad line region (BLR). In brief, the optical continuum rises rapidly and then declines following $t^{-5/3}$ (Trakhtenbrot et al. 2019), a behavior consistent with the fallback accretion rate expected in TDEs. The significant 100-day delay in broad emission line formation suggests that the BLR emerges after the outburst and likely has not yet been virialized. The subsequent rapid secular evolution of the BLR kinematics results in significant changes in the broad line profiles, including variations in the Balmer decrements, profile shapes and line widths (Li et al. 2022). Interestingly, as the optical continuum flux decreases, the width of the broad lines is also diminished, a pattern commonly observed in TDEs and attributed to a decelerating outflow (Holoien et al. 2016; Leloudas et al. 2019). Moreover, the strength of the narrow Balmer lines systematically increases by a factor of 4. In conclusion, the outburst behavior in the optical continuum and overall evolution of the broad emission lines suggest that the CLE in 1ES 1927+654 is associated with a TDE (Li et al. 2022).

Additionally, various outburst events have been detected in different AGNs over the past few decades (e.g., Graham et al. 2020; Zhang 2023). For instance, the narrow-line Seyfert 1 galaxy CSS J102913+404220 experienced multi-band outbursts around 2010, possibly also linked to a tidal disruption event (TDE). Zhang et al. (2022) found that its UV/optical continuum remained relatively constant over time, while the broad $H\alpha$ line increased in flux approximately a decade after the nuclear optical outburst. They suggested that this phenomenon might be due to the replenishment of gas and excitation in the BLR, potentially resulting from interactions with outflowing stellar debris.

At first glance, Mrk 1018 and 1ES 1927+654 appear to share similar phenomena, such as an outburst in optical continuum associated with the strong changes in their accretion rates, which illuminated the BLR and induced a full-cycle changing-look transition. However, the outburst characteristics suggest that the drastic change in the accretion rate of 1ES 1927+654 is attributed to a TDE, whereas in Mrk 1018, the outburst is most likely linked to the behavior of the accretion disk itself (for further details, see Section 3.1). That is to say, the full-cycle changing-look transitions in each AGN might result from different feeding mechanisms. Furthermore, the evolution of broad emission lines also show differences between the two sources. Specifically, the Balmer decrement of the broad line ($H\alpha/H\beta$) in

1ES 1927+654 steadily increases from 1 to 7 following the emergence of the broad lines, while in Mrk 1018, the Balmer decrement decreases from 9 to 1 as the Eddington ratio increases. Additionally, in 1ES 1927+654, the FWHM decreases with optical continuum flux, a trend commonly seen in TDEs, whereas in Mrk 1018, the FWHM displays an opposite trend. Moreover, Trakhtenbrot et al. (2019) and Li et al. (2022) revealed that the emergence of the broad Balmer line, significantly lags behind the rising optical continuum, suggesting a newly formed BLR. In contrast, Mrk 1018 showed weak broad $H\beta$ and $H\alpha$ lines ($H\beta/[O\text{ III}]\lambda 5007=0.1$) before the outburst/changing-look event, and the variation of broad $H\beta$ line follows the optical continuum changes without significant deviation from the empirical BLR radius-luminosity relation. These differences imply different physical processes: 1ES 1927+654 may elucidate the formation of the BLR (see Li et al. 2022), while Mrk 1018 may illustrate the BLR evolution during AGN turn-on or turn-off.

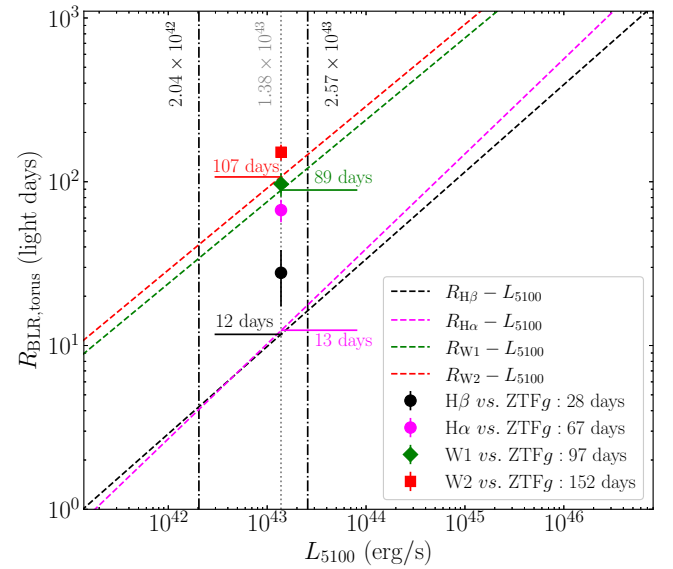


Figure 10. Relations between emission region sizes and optical luminosities. The dashed lines represent the empirical radius-luminosity relations for the $H\beta$ (in black) and $H\alpha$ (in pink) BLR (Bentz et al. 2013; Cho et al. 2023) and the torus (Chen et al. 2023b, in red and green). The colored horizontal line segments mark the sizes obtained from the corresponding empirical radius-luminosity relation (with the same color code). The vertical black dot-dashed lines denote the minimum and maximum luminosities observed during the outburst phase, while the averaged luminosity is denoted by a gray vertical dotted line. The data points represent the estimated sizes of the BLR and torus estimated from the outburst light-curve modeling.

4.2. Torus-BLR Connection

Over the past decades, great efforts have been made to establish the empirical radius-luminosity relations for selected AGN samples as shown in Figure 10 (Bentz et al. 2013; Cho

et al. 2023; Chen et al. 2023b). Such as, the $H\beta$ - and $H\alpha$ -based BLR radius-luminosity relation $R_{H\beta} = 33.6 l_{44}^{0.533}$ (Bentz et al. 2013) and $R_{H\alpha} = 38.9 l_{44}^{0.58}$ light days (Cho et al. 2023); the hot torus $W1$ - and $W2$ -band radius-luminosity relations $R_{W1} = 239 l_{44}^{0.5}$ and $R_{W2} = 289 l_{44}^{0.5}$ light days (Chen et al. 2023b), where $l_{44} = L_{5100}/10^{44} \text{ erg s}^{-1}$ with L_{5100} being the optical Luminosity at 5100 Å. These relations, with a typical intrinsic scatter of ~ 0.2 dex, provide an effective way to estimate sizes of BLR and torus for a given optical luminosity.

For the average optical luminosity of $1.38 \times 10^{43} \text{ erg s}^{-1}$ (see Table 2) during the outburst phase of Mrk 1018, we derive the expected sizes of the broad $H\beta$ and $H\alpha$ lines, $W1$ - and $W2$ -band emission regions (shown in Figure 10), corresponding to the light travel times of 12 days, 13 days, 89 days and 107 days, respectively. During this phase, the torus size of Mrk 1018 is consistent with the empirical torus radius–luminosity relation if taking into account the scatter, whereas the sizes of broad $H\beta$ and $H\alpha$ BLRs are large than the expected sizes by 0.37 and 0.75 dex, respectively. In particular, it seems that the broad $H\alpha$ BLR is close to the mid-infrared emission region. Recent reverberation mapping studies found that the broad $H\beta$ line lags are shorter than predicted from the canonical BLR radius-luminosity relation for super-Eddington AGNs (Du et al. 2016, 2018) and sub-Eddington AGNs (Grier et al. 2017; Malik et al. 2024). In contrast, in Mrk 1018, the BLR size observed during the outburst phase in turn is larger than predicted.

Three factors may explain the large BLR radius observed during the outburst phase. First, the rapid and extreme outburst can drive disk winds, creating shocks in the dense BLR and pushing it away from the central SMBH. If we assume that the 16 light-day deviation of the broad $H\beta$ emitter from the radius-luminosity relation (Bentz et al. 2013) is due to this phenomenon over a rising timescale of about two hundred days, it would require a significant radial velocity of $2.4 \times 10^4 \text{ km s}^{-1}$, which is 4 times higher than the BLR’s rotational velocity of 5475 km s^{-1} . However, the virialized nature of the BLR (as shown in Figure 8 and panel (d) of Figure 9) contradicts this possibility. Second, historical observation shows that Mrk 1018 reverted from type 1.0 to type 1.8 around 2015, suggesting that the inner BLR gases may have been depleted prior to this transition (e.g., due to accretion). Consequently, the recent outburst could ionize gases located farther from the SMBH and closer to the dust torus’s sublimation region, leading to the formation of low-ionization lines. However, the connection between the accretion flow and BLR gases remains unclear. The third possibility might be that the BLR is coupled with the dust torus, as proposed by various BLR models. For example, a tidal disruption of dusty clumps by the SMBH could form a BLR (Wang et al. 2017); The BLR model depicts two distinct emission regions associated with the dust torus (see Figure 11 of Nagoshi et al. 2024); and strong local dusty winds from the disk (i.e., FRADO, see Section 3.4) could also contribute to low-ionization emission lines (Czerny & Hryniewicz 2011). If the latter scenario is valid, the dusty wind, comprising

of low-ionization BLR gas and dust, could generate mid-infrared photons, producing low-ionization broad lines near the torus.

4.3. Robustness of Light-curve Modeling and Time Delay Measurement

After detrending, we fitted all outburst light-curve profiles using Gaussian and GE models (see Appendix A), and examined the intrinsic optical and mid-infrared color–magnitude relations during the outburst (Appendix B). Although the rising phase of the outburst was not well sampled, several factors indicate that the Gaussian modeling of these profiles is both sensible and robust. The mid-infrared outburst profiles appear symmetric. Gaussian fitting for all outburst profiles yields lower Bayesian Information Criterion (BIC) and Akaike’s Information Criterion (AIC) values compared to other models, despite similar reduced χ^2 values. Although the BLR radius from our light-curve modeling exceeds the estimate from the empirical BLR radius-luminosity relation, the obtained torus radius is well consistent with the empirical torus radius-luminosity relation (see Figure 10). By assuming that the torus is unaffected by the outburst, this suggests that light-curve modeling in mid-infrared and optical bands provides reliable measurement of torus radius. Possible explanations for the larger BLR radius are discussed in Section 4.2. We also found that the color–magnitude relations for the rising and dimming phases are consistent (Figure 7) when analyzed with Gaussian modeling data (the TDE model was excluded, see Section 3.3 and Appendix B), indicating that these outburst light-curve profiles are well-represented by Gaussian functions. Furthermore, the corrections of time delay on different bands (derived from Gaussian modeling) are likely reasonable since unreliable time-delay corrections would lead to large dispersion in these relations, such as different intercepts. In addition, if the different models are valid for describing the rising and dimming variability-behaviors, such the GE model considered in Appendix B, it leads to intricate color–magnitude relations as shown in Figure 12, characterized by different amplitudes, intercepts, and slopes. However, the underlying reasons for these complex relationships remain unclear. We anticipate that upcoming surveys, like LSST and SVOM (Czerny et al. 2023; Xu et al. 2024), will uncover more extreme events similar to those seen in Mrk 1018, facilitating a more thorough exploration of nuclear variability.

5. SUMMARY

We performed long-term spectroscopic monitoring of Mrk 1018 using Lijiang 2.4 m telescope from 2017 to 2024 to investigate the evolution of AGNs. Our observations revealed a full-cycle changing-look transition, triggered by a significant outburst from the nucleus within one year. Combining with the archival spectral data, we detected a full-cycle type transition in Mrk 1018 for the first time, encompassing Types 1.0, 1.2, 1.5, 1.8, 1.9 and 2.0, and found strong evidence that the full-cycle type transition is regulated by accretion. Our extensive investigation obtains the following findings:

1. During the full-cycle changing-look transition, the luminosity of Mrk 1018 reaches a few percent of the Eddington limit ($0.1\sim 1\%$), and the optical broad emission line exhibits a double-peaked shape. The multi-band light curves of the outburst, with a characteristic timescale of about one year, were found to be strongly correlated. The nucleus spectrum becomes bluer during the outburst. These characteristics suggest that the nucleus outburst is likely due to an instability in the accretion disk occurring in the transition region between the outer standard thin disk and an inner advection-dominated accretion flow (Sniegowska et al. 2020). Alternatively, the changing-look timescale of about one year observed around 2020 could also be attributed to a sudden inflow of surrounding gas within the Bondi accretion radius between the BLR and narrow-line region (Wang et al. 2024). For the first time, we detected a bluer-when-brighter trend in the mid-infrared, which supports the scenario of AGN-heated dust torus (Netzer 2013). We also noted that the low-ionization broad-line region is very close to the torus, which indicates that BLR may be coupled with the torus.

2. During the full-cycle type transition, we found a change in the Eddington ratio of Mrk 1018 from 2.0×10^{-5} to 0.02. This suggests a significant state change of the central engine, and implies a transition from a passive to an active state of the SMBH. Our findings reveal that the highly variable accretion rate influences the properties of the broad lines. For example, the broad-line Balmer decrement varies from about 1.5 to 9, initially rising but then declining as the Eddington ratio increases, aligning with the theoretical predictions (Netzer 1975). The broad Balmer line transitions from a single peak in Type 1.0-1.2 phase to double peaks in Type 1.5-1.8 phase and the separation of the double peak decreases with increasing Eddington ratio, which is observed for the first time. Despite significant changes in the central engine over the past 45 years, the variation in the broad-line FWHM of Mrk 1018 obeys the relation $\text{FWHM}\propto (L_{\text{bol}}/L_{\text{Edd}})^{-0.27}$, indicating that the BLR remains virialized and its global kinematics is stable (at least for the low-accretion scenario of Mrk 1018). However, the velocity dispersion σ_{line} of the broad Balmer lines shows a similar trend as the FWHM when the Eddington ratio is below ~ 0.013 (in Type 1.8-1.5 phase), but sharply increases as Eddington ratio exceeds ~ 0.013 (in Type 1.2-1.0 phase). Consequently, the ratio $\text{FWHM}/\sigma_{\text{line}}$ remains constant at an average value of 2.96 when the Eddington ratio is below ~ 0.013 , and then drops to 1.71 when the Eddington ratio exceeds this threshold. This finding suggests that the state transition of the accretion disk or the rising accretion rate might enhance the turbulent motions in the virialized BLR.

3. We estimated the virial mass of the SMBH in Mrk 1018 using the broad $H\beta$ line width (FWHM) and its time delay during the outburst phase, yielding $M_{\bullet} = (1.64 \pm 0.98) \times 10^8 M_{\odot}$. This is well consistent with the estimate from the $M_{\bullet} - \sigma_{*}$ relation $M_{\bullet} = (1.61 \pm 0.41) \times 10^8 M_{\odot}$.

Understanding the full-cycle changing-look transition and type transition is crucial for studying the feeding and evolution of AGNs. Mrk 1018 provides an ideal case for examining the physical processes involved in AGN evolution. We expect that the new observations, such as those from the Einstein Probe and the Legacy Survey of Space and Time, will unveil more extreme events similar to those observed in Mrk 1018, enhancing our understanding of the nuclear activities.

ACKNOWLEDGMENTS

We thank the referee for the useful report that improved the manuscript. This work is supported by the National Key R&D Program of China with No. 2021YFA1600404. K.X.L. acknowledges financial support from the National Natural Science Foundation of China (NSFC-12073068, 11991051, 11873048, 11703077), the Young Talent Project of Yunnan Province, the Youth Innovation Promotion Association of Chinese Academy of Sciences (2022058), the Yunnan Province Foundation (202001AT070069), and the Light of West China Program provided by Chinese Academy of Sciences (Y7XB016001), the science research grants from the China Manned Space Project with No. CMS-CSST-2021-A06. Y.R.L. acknowledges financial support from the NSFC through grant No. 12273041 and from the Youth Innovation Promotion Association CAS. LCH was supported by the National Science Foundation of China (11991052, 12233001), the National Key R&D Program of China (2022YFF0503401), and the China Manned Space Project (CMS-CSST-2021-A04, CMS-CSST-2021-A06). H.C.F. acknowledges support from National Natural Science Foundation of China (NSFC-12203096 and 12373018), Yunnan Fundamental Research Projects (grant NO. 202301AT070339), and Special Research Assistant Funding Project of Chinese Academy of Sciences. S.S.L. acknowledges support from National Natural Science Foundation of China (NSFC-12303022), Yunnan Fundamental Research Projects (grant No. 202301AT070358), and Yunnan Postdoctoral Research Foundation Funding Project. M.Y.S. acknowledges support from the National Natural Science Foundation of China (NSFC-12322303), and the National Science Foundation of Fujian Province of China (No. 2022J06002). C.C. acknowledges NSFC grant No. 12173045. This work is sponsored (in part) by the Chinese Academy of Sciences (CAS), through a grant to the CAS South America Center for Astronomy (CASSACA).

The long-term spectroscopic monitoring of Mrk 1018 has undergone through several years. We acknowledge the support of the staff of the Lijiang 2.4 m telescope. Funding for the telescope has been provided by Chinese Academy of Sciences and the People's Government of Yunnan Province.

This research makes use of data from Zwicky Transient Facility (ZTF). ZTF is supported by the National Science Foundation under grants no. AST-1440341 and AST-2034437 and a collaboration including current partners Caltech, IPAC, the Weizmann Institute for Science, the Oskar Klein Center at Stockholm University, the University of Maryland, Deutsches Elektronen-Synchrotron and Humboldt University, the TANGO Consortium of Taiwan, the University of Wisconsin at Milwaukee, Trinity College Dublin, Lawrence Livermore National Laboratories, IN2P3, University of Warwick, Ruhr University Bochum, Northwestern University and former partners the University of Washington, Los Alamos National Laboratories, and Lawrence Berkeley National Laboratories. Operations are conducted by COO, IPAC, and UW.

This research makes use of data from the Asteroid Terrestrial-impact Last Alert System (ATLAS) project. The ATLAS project is primarily funded to search for near earth asteroids through NASA grants NN12AR55G, 80NSSC18K0284, and 80NSSC18K1575; byproducts of the NEO search include images and catalogues from the survey area.

This research makes use of data products from NEOWISE. NEOWISE is a project of the Jet Propulsion Laboratory/California Institute of Technology, funded by the Planetary Science Division of the National Aeronautics and Space Administration.

APPENDIX

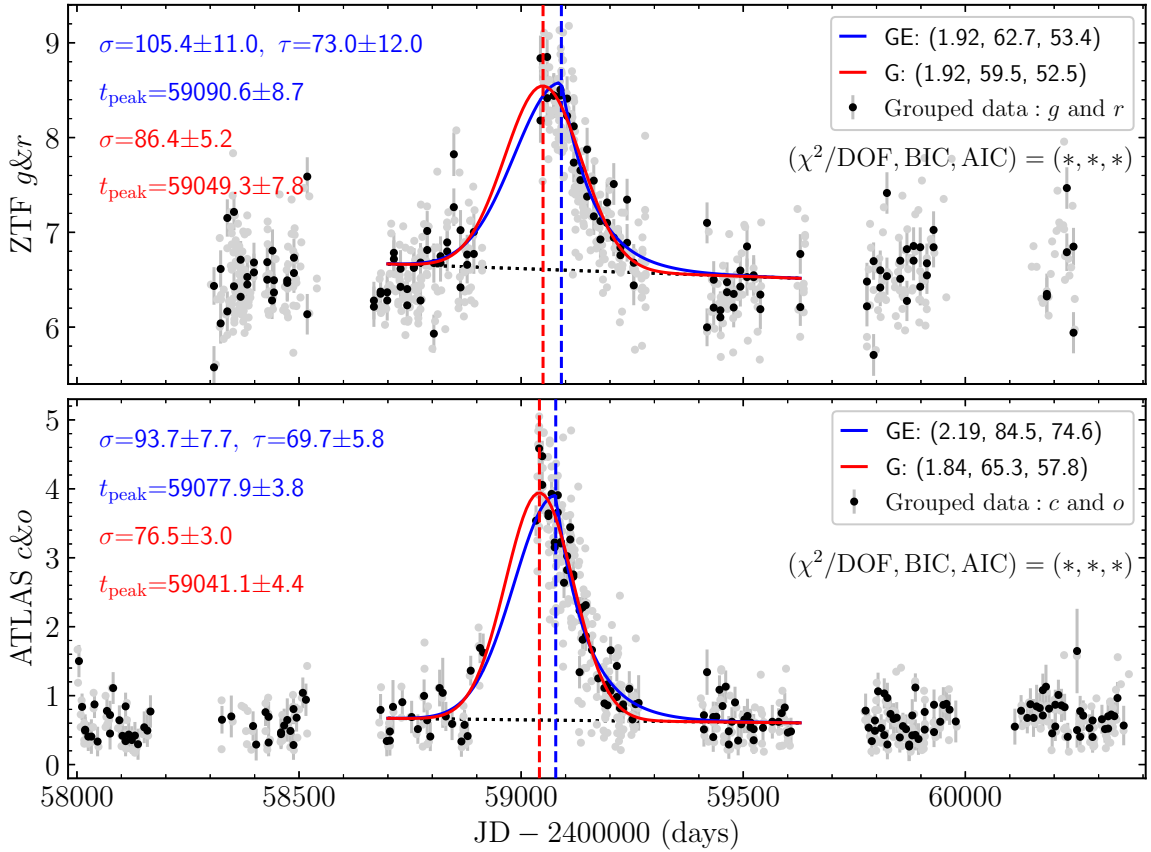


Figure 11. The light curves (in flux density) from ZTF and ATLAS along with model fitting. After subtracting the underlying trend, the outburst light-curve profiles are fitted using two models, one with Gaussian rising and exponential dimming (GE; blue lines), and the other with a single Gaussian (G; red lines). The best-fit parameters, including σ (days), τ (days) and t_{peak} (-2,400,000 days) are shown in the same color code. The vertical dashed line shows the peak position, which has the same color code with model. The fitting goodness statistics, including χ^2/dof , Bayesian Information Criterion (BIC), and Akaike's Information Criterion (AIC) are also noted. The Gaussian model yields smaller BIC and AIC values compared to the GE model.

A. OUTBURST LIGHT-CURVE MODELING AND CHARACTERISTICS

Usually, tidal disruption events (TDEs) and significant changes in accretion rate often drive extreme outburst behaviors in galactic centers (Graham et al. 2020; Zhang 2023). The power-law function is widely used to describe the dimming phase of TDEs and generally provides good fits in most cases. However, a few TDEs obviously deviate from the power-law decay and need an exponential function to fit the light curves (Yao et al. 2023). The origins of extreme accretion-driven AGN outburst over various timescales remain contentious and lack a definitive physical model. Although supernova events have been observed in some Seyfert host galaxies, there is no established precedent for such occurrences in AGN nuclei, so the supernova model is not considered here. It should be noted that, Brogan et al. (2023) reported this outburst event, mainly based on the ATLAS photometric data. They used a linear function to fit the data in the declining phase, yielding $\chi^2/\text{dof} > 60$, and also tried with a parabolic function and a power law with various power-law indexes (including $-5/3$ for a TDE outburst), all yielding $\chi^2/\text{dof} > 100$. They therefore claimed that the linear function is the best fit. By inspecting the multi-band outburst profiles, we find that the dimming phase obviously diverges from the linear trend. This prompts us to explore alternative models. We start with Gaussian rising and power-law dimming (GP model):

$$F_\lambda = A \times \begin{cases} e^{-(t-t_{\text{peak}})/2\sigma^2}, & t \leq t_{\text{peak}} \\ \left(\frac{t-t_{\text{peak}}+t_0}{t_0}\right)^p, & t > t_{\text{peak}} \end{cases} \quad (\text{A1})$$

where A represents the amplitude, t denotes the observing time, t_{peak} is the light peak time, t_0 is the power-law normalization, and p is the power-law index. However, we find that GP model fails to match the data. We then attempt to use Gaussian rising plus exponential dimming (GE model):

$$F_\lambda = A \times \begin{cases} e^{-(t-t_{\text{peak}})/2\sigma^2}, & t \leq t_{\text{peak}} \\ e^{-(t-t_{\text{peak}})/\tau}, & t > t_{\text{peak}} \end{cases} \quad (\text{A2})$$

where τ represents dimming timescale. Finally, we also try with a single Gaussian (G model) considering the evident symmetry of the mid-infrared outburst light-curve profile:

$$F_\lambda = A \times e^{-(t-t_{\text{peak}})/2\sigma^2}, t_{\text{peak}} < t \leq t_{\text{peak}} \quad (\text{A3})$$

Figure 11 presents the modeling results for merged ZTF and ATLAS light curves. The parameters for the GE and Gaussian model (except the amplitudes) are reported, along with the resulting χ^2/dof , Bayesian Information Criterion (BIC), and Akaike's Information Criterion (AIC). We find that both models yield similar values of χ^2/DOF , whereas, the BIC and AIC of GE model are slightly larger than Gaussian model. Given the nearly symmetric outburst light-curve shapes in the mid-infrared ($W1$ and $W2$ bands), we prefer to using the Gaussian model to describe the outburst light-curve profiles. Further arguments for this choice are provided in Appendix B and Section 4.3. Consequently, we present the Gaussian modeling results for the outburst light-curve profiles, including ZTF optical bands, broad Balmer lines, and mid-infrared bands in Figure 6, from which we derive the outburst characteristics listed in Table 3.

B. COLOR VS. MAGNITUDE DIAGRAMS

To analyze the color–magnitude relations in the optical and mid-infrared bands, we grouped the raw g - and r -band photometric data by a 15-day intervals and the raw $W1$ - and $W2$ -band photometric data by a six-month interval. Appendix A (also see Figure 11) suggests that the outburst light-curve profiles can be effectively modeled using either the Gaussian or GE model, with the Gaussian model yielding slightly lower BIC and AIC values. In this appendix, we examine the color–magnitude relations during the outburst phase from both models.

The results with the Gaussian models are shown in the top panels of Figure 7 (panels aa and ba; also see Appendix A and Figure 6). The second row (panels ab and bb) of Figure 7 presents the relations of the color $g-r$ versus g and $W1-W2$ versus $W1$, which are generated directly from the grouped and fitting model. The intrinsic optical color is contaminated by delayed emission lines because for Mrk 1018 ($z=0.043$), the ZTF g -band covers the broad $H\beta$ lines and ZTF r -band covers the broad $H\alpha$ lines. Additionally, the intrinsic mid-infrared color is affected by inter-band time delay. The intrinsic optical color ($g'-r'$) is derived by adjusting $g(t)-r(t)$ with a correction factor of $-2.5\log\frac{H\alpha(t-\tau_{H\alpha})}{H\beta(t-\tau_{H\beta})}$, thus $g'-r'=g(t)-r(t-\tau_r)-(-2.5\log\frac{H\alpha(t-\tau_{H\alpha})}{H\beta(t-\tau_{H\beta})})$, where τ_r , $\tau_{H\alpha}$ and $\tau_{H\beta}$ are the time delays of the ZTF r -band, broad $H\alpha$ and $H\beta$ lines with respect to the varying ZTF g -band. The intrinsic mid-infrared color ($W1'-W2'$) is obtained by correcting the inter-band time delay (τ_{W2}) between the $W2$ -band and the varying $W1$ -band, given by $W1'-W2'=W1(t)-W2(t-\tau_{W2})$. In the third row (panels ac and bc) of Figure 7, the colorized thick lines and color bars present the intrinsic color–magnitude relations for optical and mid-infrared bands during the outburst phase. In order to obtain the net color–magnitude relation that reflects the nature of the outburst phase, we removed the underlying linear variation trend from the intrinsic color–magnitude relations given above. The resulting net optical color–magnitude relation is defined as $g''-r''=g'-r'-(-2.5\log\frac{\delta r(t-\tau_r)}{\delta g(t)})$, where δr and δg represent the linear variation trends beneath the outburst light-curve

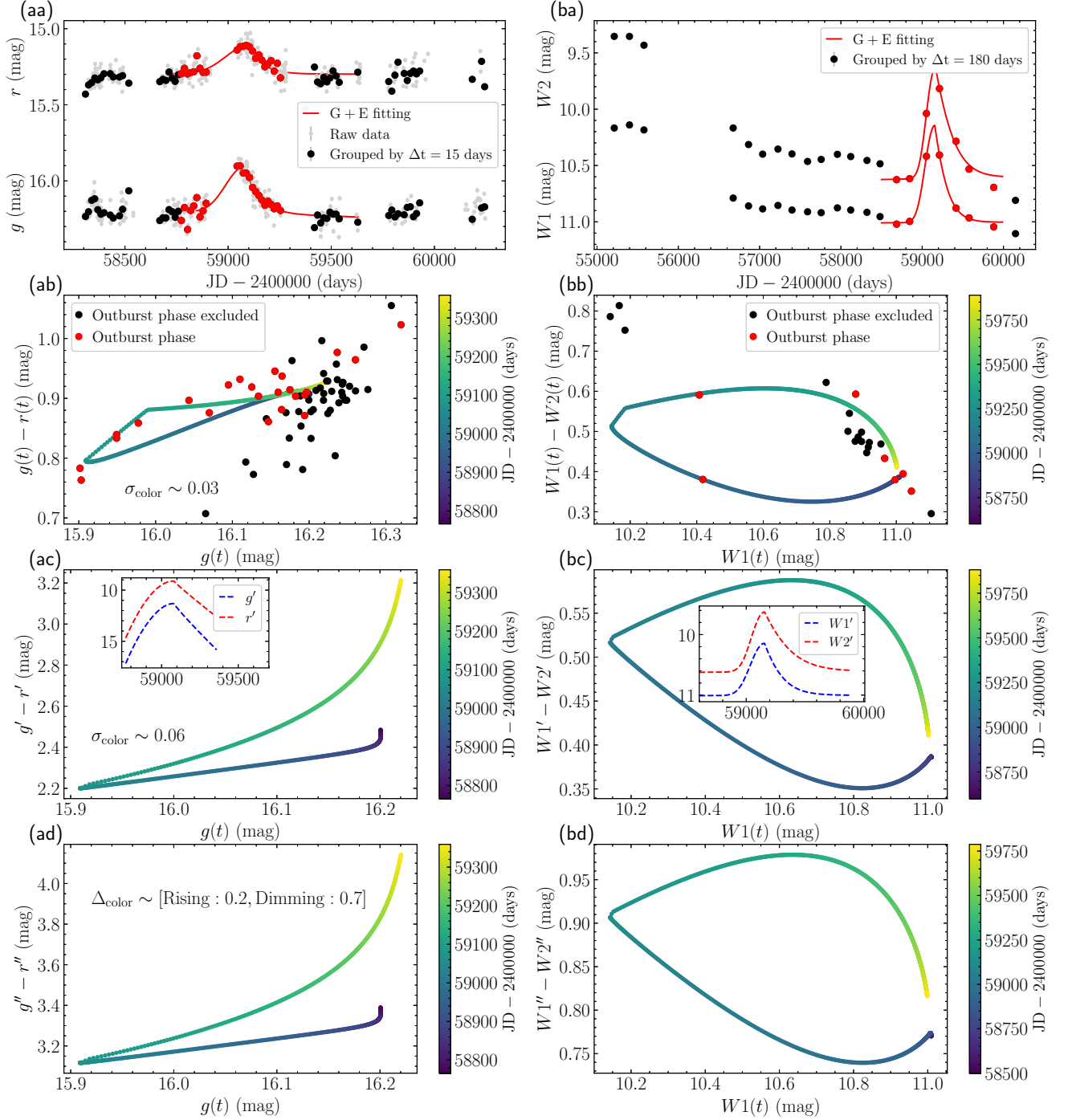


Figure 12. Same as Figure 7, but for the optical and mid-infrared color relations based on GE model (also see Appendix B).

profiles for the r - and g -bands, assuming equal zero-point flux densities for both bands. The net mid-infrared color–magnitude relation is expressed as $W1'' - W2'' = W1' - W2' - (-2.5 \log \frac{\delta_2(t - \tau_{w2})/2.43}{\delta_1(t)/8.03})$, where δ_2 and δ_1 represent the linear variation trends beneath the outburst light-curve profiles for $W2$ - and $W1$ -bands, and $2.43/8.03$ is the zero-point flux density ratio. We present net optical and mid-infrared color–magnitude relations in the bottommost row (panels ad and bd). The corresponding results from the GE model are shown in Figure 12.

We find that in the Gaussian model, the intrinsic color–magnitude relations during rising and dimming phases show nearly identical slopes and intercepts in both optical and mid-infrared bands. In contrast, in the GE model, the intrinsic color–magnitude relations in optical band show different amplitudes and slopes between the rising and dimming phases, while the mid-infrared rela-

tions shows opposite evolutionary tracks. Nonetheless, during the dimming phase, both models give consistent color–magnitude relations, with optical colors becoming redder as the source dims, suggesting these trends are model-independent. Additionally, the optical color–magnitude relation in the dimming phase does not coincide with theoretical prediction of TDEs, which typically exhibit a bluer spectrum during dimming, thereby excluding the TDE scenario in Mrk 1018.

REFERENCES

- Abazajian, K. N., Adelman-McCarthy, J. K., Agüeros, M. A., et al. 2009, *ApJS*, 182, 543. doi:10.1088/0067-0049/182/2/543
- Abramowicz, M. A., Chen, X., Kato, S., et al. 1995, *ApJL*, 438, L37. doi:10.1086/187709
- Antonucci, R. 1993, *ARA&A*, 31, 473. doi:10.1146/annurev.aa.31.090193.002353
- Barth, A. J., Bennert, V. N., Canalizo, G., et al. 2015, *ApJS*, 217, 26. doi:10.1088/0067-0049/217/2/26
- Bennert, V. N., Auger, M. W., Treu, T., et al. 2011, *ApJ*, 742, 107. doi:10.1088/0004-637X/742/2/107
- Bentz, M. C., Denney, K. D., Grier, C. J., et al. 2013, *ApJ*, 767, 149. doi:10.1088/0004-637X/767/2/149
- Bentz, M. C., Walsh, J. L., Barth, A. J., et al. 2010, *ApJ*, 716, 993. doi:10.1088/0004-637X/716/2/993
- Blandford, R. D. & McKee, C. F. 1982, *ApJ*, 255, 419. doi:10.1086/159843
- Boroson, T. A. & Green, R. F. 1992, *ApJS*, 80, 109. doi:10.1086/191661
- Brogan, R., Krumpe, M., Homan, D., et al. 2023, *A&A*, 677, A116. doi:10.1051/0004-6361/202346475
- Bruzual, G. & Charlot, S. 2003, *MNRAS*, 344, 1000. doi:10.1046/j.1365-8711.2003.06897.x
- Cai, Z.-Y., Wang, J.-X., Gu, W.-M., et al. 2016, *ApJ*, 826, 7. doi:10.3847/0004-637X/826/1/7
- Capellupo, D. M., Netzer, H., Lira, P., et al. 2015, *MNRAS*, 446, 3427. doi:10.1093/mnras/stu2266
- Chen, K. & Halpern, J. P. 1989, *ApJ*, 344, 115. doi:10.1086/167782
- Chen, Y.-J., Bao, D.-W., Zhai, S., et al. 2023a, *MNRAS*, 520, 1807. doi:10.1093/mnras/stad051
- Chen, Y.-J., Liu, J.-R., Zhai, S., et al. 2023b, *MNRAS*, 522, 3439. doi:10.1093/mnras/stad1136
- Cho, H., Woo, J.-H., Wang, S., et al. 2023, *ApJ*, 953, 142. doi:10.3847/1538-4357/ace1e5
- Cohen, R. D., Rudy, R. J., Puetter, R. C., et al. 1986, *ApJ*, 311, 135. doi:10.1086/164758
- Cutri, R. M., Wisniewski, W. Z., Rieke, G. H., et al. 1985, *ApJ*, 296, 423. doi:10.1086/163461
- Czerny, B. & Hryniewicz, K. 2011, *A&A*, 525, L8. doi:10.1051/0004-6361/201016025
- Czerny, B., Panda, S., Prince, R., et al. 2023, *A&A*, 675, A163. doi:10.1051/0004-6361/202345844
- Denney, K. D., De Rosa, G., Croxall, K., et al. 2014, *ApJ*, 796, 134. doi:10.1088/0004-637X/796/2/134
- Dong, X.-B., Wang, J.-G., Ho, L. C., et al. 2011, *ApJ*, 736, 86. doi:10.1088/0004-637X/736/2/86
- Du, P., Lu, K.-X., Zhang, Z.-X., et al. 2016, *ApJ*, 825, 126. doi:10.3847/0004-637X/825/2/126
- Du, P., Zhang, Z.-X., Wang, K., et al. 2018, *ApJ*, 856, 6. doi:10.3847/1538-4357/aaae6b
- Elitzur, M., Ho, L. C., & Trump, J. R. 2014, *MNRAS*, 438, 3340. doi:10.1093/mnras/stt2445
- Fan, Y.-F., Bai, J.-M., Zhang, J.-J., et al. 2015, *Research in Astronomy and Astrophysics*, 15, 918. doi:10.1088/1674-4527/15/6/014
- Feng, H.-C., Li, S.-S., Bai, J. M., et al. 2024, arXiv:2409.01637. doi:10.48550/arXiv.2409.01637
- Feng, H.-C., Liu, H. T., Bai, J. M., et al. 2021, *ApJ*, 912, 92. doi:10.3847/1538-4357/abefe0
- Ferrarese, L. & Merritt, D. 2000, *ApJL*, 539, L9. doi:10.1086/312838
- Gaspari, M., Tombesi, F., & Cappi, M. 2020, *Nature Astronomy*, 4, 10. doi:10.1038/s41550-019-0970-1
- Gebhardt, K., Bender, R., Bower, G., et al. 2000, *ApJL*, 539, L13. doi:10.1086/312840
- Goad, M. R., Korista, K. T., & Ruff, A. J. 2012, *MNRAS*, 426, 3086. doi:10.1111/j.1365-2966.2012.21808.x
- Graham, M. J., Kulkarni, S. R., Bellm, E. C., et al. 2019, *PASP*, 131, 078001. doi:10.1088/1538-3873/ab006c
- Graham, M. J., Ross, N. P., Stern, D., et al. 2020, *MNRAS*, 491, 4925. doi:10.1093/mnras/stz3244
- Greene, J. E. & Ho, L. C. 2005, *ApJ*, 630, 122. doi:10.1086/431897
- Greene, J. E., Strader, J., & Ho, L. C. 2020, *ARA&A*, 58, 257. doi:10.1146/annurev-astro-032620-021835
- Grier, C. J., Trump, J. R., Shen, Y., et al. 2017, *ApJ*, 851, 21. doi:10.3847/1538-4357/aa98dc
- Guo, H. & Gu, M. 2014, *ApJ*, 792, 33. doi:10.1088/0004-637X/792/1/33
- Guo, H. & Gu, M. 2016, *ApJ*, 822, 26. doi:10.3847/0004-637X/822/1/26
- Guo, W.-J., Zou, H., Fawcett, V. A., et al. 2024a, *ApJS*, 270, 26. doi:10.3847/1538-4365/ad118a
- Guo, W.-J., Zou, H., Greenwell, C. L., et al. 2024b, arXiv:2408.00402. doi:10.48550/arXiv.2408.00402
- Ho, L. C. 2008, *ARA&A*, 46, 475. doi:10.1146/annurev.astro.45.051806.110546
- Ho, L. C. 2009, *ApJ*, 699, 638. doi:10.1088/0004-637X/699/1/638

- Ho, L. C., Rudnick, G., Rix, H.-W., et al. 2000, *ApJ*, 541, 120.
doi:10.1086/309440
- Holoien, T. W.-S., Kochanek, C. S., Prieto, J. L., et al. 2016, *MNRAS*, 455, 2918. doi:10.1093/mnras/stv2486
- Hu, C., Du, P., Lu, K.-X., et al. 2015, *ApJ*, 804, 138.
doi:10.1088/0004-637X/804/2/138
- Hu, C., Li, S.-S., Guo, W.-J., et al. 2020, *ApJ*, 905, 75.
doi:10.3847/1538-4357/abc2da
- Husemann, B., Urrutia, T., Tremblay, G. R., et al. 2016, *A&A*, 593, L9. doi:10.1051/0004-6361/201629245
- Husser, T.-O., Wende-von Berg, S., Dreizler, S., et al. 2013, *A&A*, 553, A6. doi:10.1051/0004-6361/201219058
- Jarrett, T. H., Masci, F., Tsai, C. W., et al. 2013, *AJ*, 145, 6.
doi:10.1088/0004-6256/145/1/6
- Jones, D. H., Read, M. A., Saunders, W., et al. 2009, *MNRAS*, 399, 683. doi:10.1111/j.1365-2966.2009.15338.x
- Kewley, L. J., Dopita, M. A., Sutherland, R. S., et al. 2001, *ApJ*, 556, 121. doi:10.1086/321545
- Khachikian, E. Y. & Weedman, D. W. 1971, *ApJL*, 164, L109.
doi:10.1086/180701
- Kim, D.-C., Yoon, I., & Evans, A. S. 2018, *ApJ*, 861, 51.
doi:10.3847/1538-4357/aac77d
- Kollatschny, W. & Zetzl, M. 2011, *Nature*, 470, 366.
doi:10.1038/nature09761
- Kollatschny, W. & Zetzl, M. 2013, *A&A*, 549, A100.
doi:10.1051/0004-6361/201219411
- Komossa, S., Grupe, D., Marziani, P., et al. 2024, *arXiv:2408.00089*. doi:10.48550/arXiv.2408.00089
- Kong, M. & Ho, L. C. 2018, *ApJ*, 859, 116.
doi:10.3847/1538-4357/aae2a
- Korista, K. T. & Goad, M. R. 2004, *ApJ*, 606, 749.
doi:10.1086/383193
- Koss, M., Mushotzky, R., Veilleux, S., et al. 2011, *ApJ*, 739, 57.
doi:10.1088/0004-637X/739/2/57
- Kovačević, J., Popović, L. Č., & Dimitrijević, M. S. 2010, *ApJS*, 189, 15
- Krumpe, M., Husemann, B., Tremblay, G. R., et al. 2017, *A&A*, 607, L9. doi:10.1051/0004-6361/201731967
- Laha, S., Meyer, E., Roychowdhury, A., et al. 2022, *ApJ*, 931, 5.
doi:10.3847/1538-4357/ac63aa
- Leloudas, G., Dai, L., Arcavi, I., et al. 2019, *ApJ*, 887, 218.
doi:10.3847/1538-4357/ab5792
- Li, R., Ho, L. C., Ricci, C., et al. 2022, *ApJ*, 933, 70.
doi:10.3847/1538-4357/ac714a
- Li, S.-S., Feng, H.-C., Liu, H. T., et al. 2024, *arXiv:2407.05414*.
doi:10.48550/arXiv.2407.05414
- Liu, W.-J., Lira, P., Yao, S., et al. 2021, *ApJ*, 915, 63.
doi:10.3847/1538-4357/abf82c
- Li, Y.-R., Wang, J.-M., Hu, C., et al. 2014, *ApJL*, 786, L6.
doi:10.1088/2041-8205/786/1/L6
- Lu, K.-X., Bai, J.-M., Wang, J.-M., et al. 2022, *ApJS*, 263, 10.
doi:10.3847/1538-4365/ac94d3
- Lu, K.-X., Bai, J.-M., Zhang, Z.-X., et al. 2019a, *ApJ*, 887, 135.
doi:10.3847/1538-4357/ab5790
- Lu, K.-X., Wang, J.-G., Zhang, Z.-X., et al. 2021a, *ApJ*, 918, 50.
doi:10.3847/1538-4357/ac0c78
- Lu, K.-X., Zhao, Y., Bai, J.-M., et al. 2019c, *MNRAS*, 483, 1722.
doi:10.1093/mnras/sty3229
- Lu, K.-X., Zhang, Z.-X., Huang, Y.-K., et al. 2021b, *Research in Astronomy and Astrophysics*, 21, 183.
doi:10.1088/1674-4527/21/7/183
- Lyu, B., Yan, Z., Yu, W., et al. 2021, *MNRAS*, 506, 4188.
doi:10.1093/mnras/stab1581
- MacLeod, C. L., Ross, N. P., Lawrence, A., et al. 2016, *MNRAS*, 457, 389. doi:10.1093/mnras/stv2997
- Markwardt, C. B. 2009, *Astronomical Data Analysis Software and Systems XVIII*, 411, 251. doi:10.48550/arXiv.0902.2850
- Matt, G., Guainazzi, M., & Maiolino, R. 2003, *MNRAS*, 342, 422.
doi:10.1046/j.1365-8711.2003.06539.x
- Ma, Y.-S., Li, S.-J., Gu, C.-S., et al. 2023, *MNRAS*, 522, 5680.
doi:10.1093/mnras/stad1377
- Malik, U., Sharp, R., Penton, A., et al. 2024, *MNRAS*, 531, 163.
doi:10.1093/mnras/stae1154
- McElroy, R. E., Husemann, B., Croom, S. M., et al. 2016, *A&A*, 593, L8. doi:10.1051/0004-6361/201629102
- McGill, K. L., Woo, J.-H., Treu, T., et al. 2008, *ApJ*, 673, 703.
doi:10.1086/524349
- McLure, R. J. & Dunlop, J. S. 2004, *MNRAS*, 352, 1390.
doi:10.1111/j.1365-2966.2004.08034.x
- Mereghetti, S., Balman, S., Caballero-Garcia, M., et al. 2021, *Experimental Astronomy*, 52, 309.
doi:10.1007/s10686-021-09809-6
- Merloni, A., Dwelly, T., Salvato, M., et al. 2015, *MNRAS*, 452, 69.
doi:10.1093/mnras/stv1095
- Moran, E. C., Halpern, J. P., & Helfand, D. J. 1996, *ApJS*, 106, 341. doi:10.1086/192341
- Naddaf, M. H. & Czerny, B. 2022, *A&A*, 663, A77.
doi:10.1051/0004-6361/202142806
- Nagoshi, S., Iwamuro, F., Yamada, S., et al. 2024, *MNRAS*, 529, 393. doi:10.1093/mnras/stae319
- Nelson, C. H. & Whittle, M. 1996, *ApJ*, 465, 96.
doi:10.1086/177405
- Netzer, H. 1975, *MNRAS*, 171, 395. doi:10.1093/mnras/171.2.395
- Netzer, H. 2013, *The Physics and Evolution of Active Galactic Nuclei*, by Hagai Netzer, Cambridge, UK: Cambridge University Press, 2013
- Netzer, H. 2015, *ARA&A*, 53, 365.
doi:10.1146/annurev-astro-082214-122302
- Oknyansky, V. L., Winkler, H., Tsygankov, S. S., et al. 2019, *MNRAS*, 483, 558. doi:10.1093/mnras/sty3133

- Osterbrock, D. E. 1977, *ApJ*, 215, 733. doi:10.1086/155407
- Osterbrock, D. E. 1978, *Proceedings of the National Academy of Science*, 75, 540. doi:10.1073/pnas.75.2.540
- Osterbrock, D. E. 1981, *ApJ*, 249, 462. doi:10.1086/159306
- Osterbrock, D. E. & Ferland, G. J. 2006, *Astrophysics of gaseous nebulae and active galactic nuclei*, 2nd. ed. by D.E. Osterbrock and G.J. Ferland. Sausalito, CA: University Science Books, 2006
- Panda, S. & Śniegowska, M. 2024, *ApJS*, 272, 13. doi:10.3847/1538-4365/ad344f
- Panessa, F. & Bassani, L. 2002, *A&A*, 394, 435. doi:10.1051/0004-6361:20021161
- Park, D., Barth, A. J., Ho, L. C., et al. 2022, *ApJS*, 258, 38. doi:10.3847/1538-4365/ac3f3e
- Park, D., Woo, J.-H., Treu, T., et al. 2012, *ApJ*, 747, 30. doi:10.1088/0004-637X/747/1/30
- Penston, M. V. & Perez, E. 1984, *MNRAS*, 211, 33P. doi:10.1093/mnras/211.1.33P
- Peterson, B. M. 1993, *PASP*, 105, 247. doi:10.1086/133140
- Peterson, B. M., Ferrarese, L., Gilbert, K. M., et al. 2004, *ApJ*, 613, 682. doi:10.1086/423269
- Ren, W., Wang, J., Cai, Z., et al. 2022, *ApJ*, 925, 50. doi:10.3847/1538-4357/ac3828
- Ricci, C. & Trakhtenbrot, B. 2023, *Nature Astronomy*, 7, 1282. doi:10.1038/s41550-023-02108-4
- Runnoe, J. C., Cales, S., Ruan, J. J., et al. 2016, *MNRAS*, 455, 1691. doi:10.1093/mnras/stv2385
- Sakata, Y., Morokuma, T., Minezaki, T., et al. 2011, *ApJ*, 731, 50. doi:10.1088/0004-637X/731/1/50
- Shakura, N. I. & Sunyaev, R. A. 1973, *A&A*, 24, 337
- Shapovalova, A. I., Popović, L. Č., Burenkov, A. N., et al. 2010, *A&A*, 509, A106. doi:10.1051/0004-6361/200912311
- Shappee, B. J., Prieto, J. L., Grupe, D., et al. 2014, *ApJ*, 788, 48. doi:10.1088/0004-637X/788/1/48
- Sheng, Z., Wang, T., Jiang, N., et al. 2017, *ApJL*, 846, L7. doi:10.3847/2041-8213/aa85de
- Śniegowska, M., Czerny, B., Bon, E., et al. 2020, *A&A*, 641, A167. doi:10.1051/0004-6361/202038575
- Stern, J. & Laor, A. 2012a, *MNRAS*, 423, 600. doi:10.1111/j.1365-2966.2012.20901.x
- Stern, J. & Laor, A. 2012b, *MNRAS*, 426, 2703. doi:10.1111/j.1365-2966.2012.21772.x
- Strateva, I. V., Strauss, M. A., Hao, L., et al. 2003, *AJ*, 126, 1720. doi:10.1086/378367
- Sulentic, J. W., Marziani, P., Zamanov, R., et al. 2002, *ApJL*, 566, L71. doi:10.1086/339594
- Sun, M., Grier, C. J., & Peterson, B. M. 2018, *Astrophysics Source Code Library*. ascl:1805.032
- Tonry, J. L., Denneau, L., Heinze, A. N., et al. 2018, *PASP*, 130, 064505. doi:10.1088/1538-3873/aabadf
- Trakhtenbrot, B., Arcavi, I., MacLeod, C. L., et al. 2019, *ApJ*, 883, 94. doi:10.3847/1538-4357/ab39e4
- Tran, H. D., Lyke, J. E., & Mader, J. A. 2011, *ApJL*, 726, L21. doi:10.1088/2041-8205/726/2/L21
- Trippe, M. L., Crenshaw, D. M., Deo, R. P., et al. 2010, *ApJ*, 725, 1749. doi:10.1088/0004-637X/725/2/1749
- Urry, C. M. & Padovani, P. 1995, *PASP*, 107, 803. doi:10.1086/133630
- Véron-Cetty, M.-P., Joly, M., & Véron, P. 2004, *A&A*, 417, 515
- Véron-Cetty, M.-P., Véron, P., & Gonçalves, A. C. 2001, *A&A*, 372, 730. doi:10.1051/0004-6361:20010489
- Veronese, S., Vignali, C., Severgnini, P., et al. 2024, *A&A*, 683, A131. doi:10.1051/0004-6361/202348098
- Wang, C.-J., Bai, J.-M., Fan, Y.-F., et al. 2019, *Research in Astronomy and Astrophysics*, 19, 149. doi:10.1088/1674-4527/19/10/149
- Wang, J.-M., Du, P., Brotherton, M. S., et al. 2017, *Nature Astronomy*, 1, 775. doi:10.1038/s41550-017-0264-4
- Wang, J., Xu, D. W., Cao, X., et al. 2024, *ApJ*, 970, 85. doi:10.3847/1538-4357/ad4d89
- Winkler, H. 1992, *MNRAS*, 257, 677. doi:10.1093/mnras/257.4.677
- Wright, E. L., Eisenhardt, P. R. M., Mainzer, A. K., et al. 2010, *AJ*, 140, 1868. doi:10.1088/0004-6256/140/6/1868
- Wu, J., Wu, Q., Xue, H., et al. 2023, *ApJ*, 950, 106. doi:10.3847/1538-4357/acce9e
- Xu, D. W., Komossa, S., Grupe, D., et al. 2024, *Universe*, 10, 61. doi:10.3390/universe10020061
- Yang, Q., Wu, X.-B., Fan, X., et al. 2018, *ApJ*, 862, 109. doi:10.3847/1538-4357/aaca3a
- Yao, Y., Ravi, V., Gezari, S., et al. 2023, *ApJL*, 955, L6. doi:10.3847/2041-8213/acf216
- Zeltyn, G., Trakhtenbrot, B., Eracleous, M., et al. 2024, *ApJ*, 966, 85. doi:10.3847/1538-4357/ad2f30
- Zhang, W. J., Shu, X. W., Sheng, Z. F., et al. 2022, *A&A*, 660, A119. doi:10.1051/0004-6361/202142253
- Zhang, X.-G. 2023, *MNRAS*, 526, 6015. doi:10.1093/mnras/stad3153
- Zhou, H., Shi, X., Yuan, W., et al. 2019, *Nature*, 573, 83. doi:10.1038/s41586-019-1510-y